https://doi.org/10.5194/esurf-2020-20
Preprint. Discussion started: 3 April 2020

Earth Surface Dynamics Discussions

Inertial drag and lift forces for coarse grains on rough alluvial beds

Georgios Maniatis[1], Trevor Hoey[2], Rebecca Hodge[3], Dieter Rickenmann[4], and Alexandre Badoux[4]

[1]School of Environment and Technology, University of Brighton, UK
[2]Department of Civil and Environmental Engineering, Brunel University London, UK
[3]Department of Geography, Durham University, UK
[4]Swiss Federal Institute WSL

Correspondence: Georgios Maniatis (g.maniatis@brighton.ac.uk)

Abstract. Quantifying the force regime that controls the transport of a single grain during fluvial transport has historically been proven difficult. Inertial Micro Mechanical and Electrical Sensors (MEMS) sensors (sensor-assemblies that mainly comprise micro-accelerometers and gyroscopes) can be applied to this problem using a “smart-pebble": a mobile Inertial Measurement Unit (IMU) enclosed in a stone-like assembly that can measure directly the forces of sediment transport (and consequently metrics such as grain velocities, positions, and kinetic energies). Today, twenty years after this idea was introduced in the literature, it is accepted that there is potential in calculating directly inertial single pebble dynamics for short time scales (after consistent calibration and analysis) despite limitations in the accuracy of MEMS sensors that are suitable for this issue. This paper introduces and tests a theoretical framework that connects the IMU measurements with existing force balance equations for sediment grains on a riverbed. IMUs were embedded in two different grain shapes and used in flume experiments in which flow was increased until the grain moved. The data were then processed to calculate the threshold force for entrainment resulting to the statistical approximation of inertial impulse thresholds for both the lift and drag components of grain inertial dynamics. An ellipsoid IMU was then deployed in a series of *in situ* experiments in a steep stream (Erlenbach, Switzerland). The inertial dynamics provide a direct measurement of the resultant forces on sediment particles which quantifies: a) the effect of grain shape; and b) the effect of varied intensity hydraulic forcing on the motion of coarse sediment grains during bed-load transport. Lift impulses exert a significant control on the motion of the ellipsoid across hydraulic regimes and despite the occurrence of higher magnitude and duration drag impulses. The first order statistical generalisation of the results suggests that the transport of the ellipsoid is characterised by no-mobility states and that the majority of mobility states is controlled by lift impulses.

1 Introduction

River sediment transport is a critical process in landscape evolution (Tucker and Hancock, 2010), controls river morphology and ecology (Recking et al., 2015) and affects river engineering (Van Rijn, 1984). The study of the two-way relationship between transport processes and the corresponding morphology has a long history (e.g. Gilbert and Murphy, 1914), using approaches and mathematical conceptualisations that range from deterministic (e.g. Gilbert and Murphy, 1914; Shields, 1936; Ali and Dey, 2016) to probabilistic (e.g. Einstein, 1937; Grass, 1970; Ancey et al., 2008).

https://doi.org/10.5194/esurf-2020-20
Preprint. Discussion started: 3 April 2020

Fluvial sediment transport is a multi-variate two-phase flow defined by a range of interacting complex subprocesses affected by: (a) hydraulics (Kline et al., 1967; Nelson et al., 1995; Papanicolaou et al., 2002); (b) sediment properties and arrangement (Ashida and Michiue, 1971; Komar and Li, 1988; Kirchner et al., 1990; Buffington et al., 1992; Hodge et al., 2013; Prancevic and Lamb, 2015); (c) flow history across time scales (Shvidchenko and Pender, 2000; Diplas et al., 2008; Valyrakis et al., 2010; Phillips et al., 2018; Masteller et al., 2019); and, (d) biological and chemical processes that can rearrange or stabilise sediment (Johnson et al., 2011; Vignaga et al., 2013; Johnson, 2016).

To analyse the motion of a grain resting on a riverbed that is sheared by a turbulent flow (Dey and Ali, 2018), a large group of laboratory and theoretical studies use an implicit (fixed) reference frame and historically such analyses have been deterministic (implementing a single threshold shear stress or force at which grains are entrained, Gilbert and Murphy, 1914; Shields, 1936; Yalin, 1963; Iwagaki, 1956; Ikeda, 1982; Dey, 1999). Separately, stochastic descriptions capture better the complex particle-fluid interplay since the highly intermittent near bed turbulence (a significant driver of grain motion) is inherently stochastic (Einstein, 1937; Grass, 1970; Papanicolaou et al., 2002; Marion and Tregnaghi, 2013). Coupled with advances in monitoring techniques (e.g. Papanicolaou et al., 2002; Fathel et al., 2016), stochastic treatments have led to Lagrangian, primarily numerical, formulations being applied to the full range of motion (McEwan et al., 2004; Bialik et al., 2015). The term Lagrangian in the literature of sediment transport is borrowed from fluid mechanics and is used to mean that sediment flow is observed from the perspective of individual mobile sediment grains (equivalent to fluid “parcels of flow") and not a fixed time and space domain (as in traditional approaches using fixed x,y,z co-ordinates, which are referred to as Eulerian). The turbulence impulse approach (Diplas et al., 2008; Valyrakis et al., 2010; Celik et al., 2010) is often cateogrised as a stochastic approach (Dey and Ali, 2018) since the stochastic nature of local turbulence is accounted for by the integration of turbulent forces acting on the grain over time (the exact definition of turbulence impulse). However, the grain forces are treated deterministically and through a detailed treatment of the force balance during incipient motion. Finally, the spatio-temporal approach (Coleman and Nikora, 2008) is different as the equations of motion are applied separately for the fluid (in a spatially averaged domain) and the sediment particles, linking the mode of transport with the scales of turbulence (Bialik et al., 2015).

Field experiments tracing individual sediment grains are in principle Lagrangian (Hassan and Roy, 2016). Lagrangian analytical models have been developed following advances in monitoring techniques that allow tracking of individual grains, including magnetic (e.g. Schmidt and Ergenzinger, 1992; Hassan et al., 2009) and RFID tracers (e.g. Schneider et al., 2014; Tsakiris et al., 2015). An important milestone in the development of Lagrangian approaches for sediment transport was the introduction of Discrete Particle Modelling techniques in simulations (McEwan et al., 2001, 2004) which opened up the prospect for upscaling the Lagrangian metrics.

Lagrangian measurements find direct application in coarse grain gravel bed and bedrock river environments (e.g. Hassan et al., 1992, 2009; Ferguson et al., 2002; Hodge et al., 2011; Liedermann et al., 2012) and the morphological impact of Lagrangian dynamics in those environments (i.e. the movement of individual grains) is pronounced (Hodge et al., 2011). For example, the inertia of the typically larger particles transported in these streams has been identified as one of the main factors contributing to the over-prediction of transport rates (Buffington and Montgomery, 1997). Equally important is the lack of information on the energy transfer between these large particles and the river bed, particularly during impact. Recent experiments (Gimbert et al., 2019), show how this energy transfer can be inferred from seismic measurements, opening the way for testing hypotheses that relate to river reach scale processes (eg. Burtin et al., 2014). Finally, for a complete understanding of these interactions, the energy generated by the rotational component of grain movement cannot be ignored (Niño and García, 1998).

A particular advance in monitoring technology has been the development of sediment grain scale inertial sensors which provide high frequency data on accelerations and angular velocities experienced by grains during entrainment and motion (Kularatna et al., 2006; Akeila et al., 2010; Frank et al., 2015; Maniatis et al., 2013; Gronz et al., 2016; Maniatis et al., 2017). These applications became possible after the development of compact MEMS (Micro Electrical Mechanical Sensors) Inertial Measurement Units (IMUs), assemblies of 3D MEMS accelerometers and 3D MEMS gyroscopes, which overcome many technical difficulties posed by older instrumentation (Ergenzinger and Jupner, 1992; Spazzapan et al., 2004). The goal is the development of an IMU based sensor assembly (IMU enclosed in a grain or a purpose specific grain shaped artificial enclosure) that can successfully measure grain dynamics.

MEMS-IMU sensors measure forces within the grains, ideally at the centre of mass if the sensors are correctly centred on this point. Data collected from within grains undergoing transport has potential to describe the timing of motion, forces acting on the grain and grain location. As a grain moves, it's centre of mass moves and so the reference point for the force measurements is mobile. The latter means that the IMU measurements need to be transformed to an observation of motion that can be understood by an observer (an IMU accelerometer at rest is a non-inertial frame “fixed" within the mobile body frame of the sensor assembly).

In theory, the accelerations recorded by the IMU could be integrated to calculate grain velocity and integrated again to reveal location. However, real fixed ('strap-down') IMUs based on MEMS are not suitable for these integrations since the data contain several sources of uncertainty including signal noise and nano-scale mis-alignment of sensor axes. In practice, with sensors that are cheap enough to be deployed in large numbers, the accumulation of errors means that they cannot be used for 3D tracking of long term unconstrained motions (Woodman, 2007; Kok et al., 2017; VectorNav, 2016). This problem is well known in both the fields of navigation and electrical engineering and the modelling of IMU errors is a significant research area (Zekavat and Buehrer, 2011) since the applications of this technology are numerous (Gebre-Egziabher et al., 1998; Grewal et al., 2007).

For sediment transport, the inability to derive unrestricted positional information has limited significantly the use of IMU sensors in the field. Even the most recent IMU laboratory deployments are best considered to be preliminary (e.g. Constantinescu et al., 2016) with the exemption of Gimbert et al. (2019) who use accelerometers as inertial impact sensors to complement seismic measurements. For field deployments, relevant sensors have to date only been used as start and stop motion sensors (Olinde and Johnson, 2015).

The first goal of this paper is to introduce a simple rigid body model that connects measurements derived from an idealised IMU with existing models for grain motion. For this model to be successful, it is necessary to resolve the IMU body frame dynamics to the reference frame of motion (flume or riverbed). This resolution allows the inertial measurements to be related to the hydraulic forces and the theoretical thresholds of motions as defined in the literature. The second goal is to introduce the calculation of inertial impulses over the drag and lift thresholds of motion, following the example of Diplas et al., 2008, for grain entrainments and short transport events. The calculations are performed for a set of flume entrainment observations using two sensor assemblies: one spherical and one ellipsoid-shaped. We apply the same analysis to a time series of successive transport events measured with the ellipsoid sensor in a steep alpine river (Erlenbach, Switzerland), calculating the force regime and the generated impulses during grain motion *in situ*. Finally, we discuss how the combined dataset (flume and *in situ* experiments) for the ellipsoid sensor can be used for bootstrap calculations leading to the generalisation of the derived measurements.

2 Frames of reference, rotations and IMU measurements

To discuss the measurements recorded by an IMU, and particularly the measurements from an accelerometer and a gyroscope, it is necessary to introduce three basic frames of reference and select one of the many representations for arbitrary rotations in 3D.

The following assumptions/ simplifications are used throughout this study:

– due to the small scale (10^{-1} to 10^{1}m, typically) motion of sediment grains, an Earth frame (one that coincides with the inertial frame as defined below, but rotates with the Earth) is not defined. Also, the angular velocity of the earth (approximately $7.29 \cdot 10^{-5}$ $\mathrm{rad.s^{-1}}$) is ignored.

– for the same reason, the non-gravitational fictitious forces (such as the Coriolis effect) are ignored.

– for the mathematical derivations, ideal IMUs (no error accumulation is considered) and perfectly aligned sensor assemblies are assumed. The errors associated with IMUs and especially with the magnitude of the integration errors are presented in relevant electrical engineering sources (eg. Kok et al., 2017). For the sensors deployed in this study, the calibration and the filtering procedure are summarized in Maniatis (2016) (chapter 6).

We define the body frame b as the coordinate frame of the moving IMU. For an ideal IMU the origin of this frame is located exactly at the center of both the accelerometer and the gyroscope and this center falls precisely on the center of mass of the complete sensor assembly (Maniatis et al., 2013, 2017).

The local geographical frame r is the stationary frame within which hydrodynamics and grain forces are analysed. This is the reference frame used implicitly for all the single grain motion studies (Dey and Ali, 2018). For laboratory experiments, the r_x-r_y plane is exactly parallel to the flume bed and the r_z direction is normal to the bed. For the field experiments this alignment will be an approximation due to variations of the local topography.

The inertial frame i is a stationary frame. Strap-down IMUs measure acceleration and angular velocity changes in response to this frame and its origin lies at the center of the Earth.

Transforming information between these three reference frames is non-trivial, and a widely-used method to represent the change between them is to apply quaternions (Hamilton, 1844; Diebel, 2006). Quaternions are an extension of complex numbers used in the description of 3D mechanics, particularly 3D rotations. They are considered the most efficient description of

https://doi.org/10.5194/esurf-2020-20
Preprint. Discussion started: 3 April 2020

unrestricted 3D rotations, as they are free from numerical errors that occur when other representations are used (such as the Gimbal Lock error associated with rotations expressed by Euler Angles, Appendix E2). A typical introduction to quaternions can be found in Valenti et al. (2015) and we follow that primer for a brief introduction to quaternion algebra in Appendix E1.

A unit quaternion ${}^B_A q$ defines a rotation from frame A to frame B and successive rotations are represented by quaternion multiplication. For each ${}^B_A q$, a Direction Cosine Matrix (DCM) $R({}^B_A q)$ is defined as a function of ${}^B_A q$ components (equation E11) which also represents a rotation from frame A to B . If ${}^B v$, ${}^A v$ are observations of the vector v in frames B and A respectively, they are related through the following typical matrix operation:

$$ {}^B v = R({}^B_A q)\, {}^A v \tag{1} $$

If the frames A and B are relatively static (such as the inertial frame i in relation to the local geographic frame r) then both ${}^B_A q$ and $R({}^B_A q)$ are explicit. If B is rotating in relation to A (such as the body frame b in relation to the inertial frame i), ${}^B_A q$ and the corresponding $R({}^B_A q)$ need to be recursively updated. The transition quaternion $\tilde{q}$ between two successive poses is defined by the applied angular velocity as:

$$ \tilde{q} = \left[\cos\frac{\|\omega\|\delta t}{2} \;\; \sin\frac{\|\omega\|\delta t}{2}\frac{\omega_{bx}}{\|\omega\|} \;\; \sin\frac{\|\omega\|\delta t}{2}\frac{\omega_{by}}{\|\omega\|} \;\; \sin\frac{\|\omega\|\delta t}{2}\frac{\omega_{bz)}}{\|\omega\|} \right]^T \tag{2} $$

where $\omega_{bx}, \omega_{by}, \omega_{bz}$ are angular velocities observed along the b_x, b_y, b_z body frame axes respectively by the 3D gyroscope, $\|\omega\| = \sqrt{\omega_{bx}^2 + \omega_{by}^2 + \omega_{bz}^2}$ is the norm of angular velocities and δt the time of rotation, set here equal to the frequency of the IMU measurements.

Equation 2 is part of the direct multiplication method (Whitmore, 2000; Zhao and van Wachem, 2013) and the updated quaternion ${}^B_A q'$ is derived as:

$$ {}^B_A q' = {}^B_A q \bigotimes \tilde{q} \tag{3} $$

with the operation $\bigotimes$ denoting quaternion multiplication (equation E4). After each update ${}^B_A q'$ is set as ${}^B_A q$.

Inertial accelerometers measure the proper acceleration a_b applied within the body frame b. These accelerations will include gravitational acceleration, a uniform force in the inertial frame i. To derive the linear acceleration in the inertial frame i it is necessary to rotate the body frame measurement to the intertial frame and then to subtract gravitational acceleration. For this

https://doi.org/10.5194/esurf-2020-20
Preprint. Discussion started: 3 April 2020

rotation the recursively updated $R({}^i_b q')$ DCM is used after calculating the ${}^i_b q'$ through equation 3. The linear acceleration in the local geographical frame r is then given by:

$$a_r = R({}^r_i q)(R({}^i_b q')a_b - g) \tag{4}$$

where $a_b = [a_{bx}\ a_{by}\ a_{bz}]^T$ is the vector of the b frame accelerometer measurements, and $R({}^r_i q)$ the explicit DCM that rotates the accelerations from i to r derived from the quaternion ${}^r_i q$. As sediment transport velocities are very small compared with the speed of light, relativistic effects are ignored and the linear acceleration a_r defines the magnitude and direction of the resultant force. This is the force that determines the kinetic state of a body as its force balance is resolved.

3 A Newton - Euler regime for sediment motion

A significant implication of using inertial measurements is that they allow forces and turning moments to be calculated directly as applied to the centre of mass of the moving object. This type of parametrisation is found in the literature of rigid body dynamics as the Newton - Euler model (O'Reilly, 2008). For a spherical particle resting on identical size densely packed spheres, irrespective of the degree of exposure to the flow, the Newton-Euler regime is defined as follows:

$$\sum F = F_{Dr} + F_{Gr} + F_{Lr} = m \begin{bmatrix} a_{rx} \\ a_{ry} \\ a_{rz} \end{bmatrix} \tag{5}$$

$$\sum T = F_R \times \frac{d}{2} = I_{cm} \begin{bmatrix} \alpha_{bx} \\ \alpha_{by} \\ \alpha_{bz} \end{bmatrix} \tag{6}$$

where F_{Dr} is the drag force exerted by the flow on the particle and F_L is the lift force generated by the flow, both analysed in the r frame. The term T represents the torque and term F_{Gr} defines the gravity related forces rotated in the r frame as:

$$F_{Gr} = R({}^r_i q)W_s f_v \tag{7}$$

W_s is the immersed weight of the spherical particle equal to $m_b g$, where m_b is its immersed mass (Papanicolaou et al., 2002) and g is the acceleration of gravity, both acting at its centre of mass. $f_v = 1 + [0.5\rho/(\rho_s - \rho)]$ accounts for the hydrodynamic mass effect (Papanicolaou et al., 2002; Celik et al., 2010) and ρ, ρ_s are the densities of the water and the particle, respectively. For our ellipsoid, we calculate F_{Gr} assuming a sphere with the same volume as the ellipsoid, since resolving the hydrodynamic mass coefficient for an ellipsoid in 3D is beyond the scope of this work.

https://doi.org/10.5194/esurf-2020-20
Preprint. Discussion started: 3 April 2020

For the balance of torques (Equation 6), F_R is the sum of surrounding grain forces applied on the surface of the target particle and d is the particle diameter.

For the right hand elements of Equations 5 and 6, m is the particle mass, I_{cm} is the moment of inertia (uniform for a sphere and equal to $md^2/10$), a_{rx}, a_{ry}, a_{rz} are linear accelerations resolved in r through Equation 4 and α_{bx}, α_{by}, α_{bz} are rotational accelerations such that:

$$\begin{bmatrix}\alpha_{bx} & \alpha_{by} & \alpha_{bz}\end{bmatrix}^T = \begin{bmatrix}\frac{d\omega_{bx}}{dt} & \frac{d\omega_{by}}{dt} & \frac{d\omega_{by}}{dt}\end{bmatrix}^T \tag{8}$$

where ω_{bx},ω_{by} and ω_{bz} are angular velocities within the body frame reference frame as recorded by gyroscope measurements.

Although this work focuses on the calculation of inertial impulses, for completeness we note that if $a_r = [a_{rx}\ a_{ry}\ a_{rz}]^T$ is the 3D vector of linear acceleration in the r reference frame, grain linear velocities can be calculated by single integration (velocity in the r frame is $\upsilon_r(t) = \upsilon_r(0) + \int_0^t a_r(t)\,dt$) and the total kinetic energy of the grain motion by using the norms of linear and angular velocities (kinetic energy is $K = \frac{1}{2}m\|\upsilon_r\|^2 + \frac{1}{2}I_{cm}\|\omega_b\|^2$ with $\frac{1}{2}m\|\upsilon_r\|^2$ being the translational and $\frac{1}{2}I_{cm}\|\omega_b\|^2$ the rotational component).

4 Inertial measurements and the linear force threshold of motion

The Newton-Euler model describes the motion of a particle but this needs to be related to existing grain incipient motion models. For a particle that is fully exposed to shear turbulent flow, as is typically assumed in theories of grain entrainment (Celik et al., 2010), the focus is on the forces that act on the centre of mass of the particle (linear forces) as defined in equation 5. Hereafter, those forces are grouped into drag forces parallel to the bed and lift forces normal to the bed for simplicity (all resolved in the r frame). The force threshold of motion regime is defined for $a_r = [0\ \ 0\ \ 0]^T$, representing a state where the force balance is not resolved (a resultant force $\sum F$ of equation 5 equal to 0).

Let $F_{Dr} = [F_{Drx}\ \ F_{Dry}\ \ 0]^T$ and $F_{Lr} = [0\ \ 0\ \ F_{Lrz}]^T$ be, respectively, the 3D drag and lift force components of Equation 5 rotated in the r frame. If $F_{Gr} = [F_{Grx}\ \ F_{Gry}\ \ F_{Grz}]$ (equation 7), then the threshold condition for the forces resolved on the $x_r - y_r$ plane parallel to the bed is defined as:

$$\sum F_{xyr} = F_{Dr} + \sum F_{Gxyr} \geq 0 \tag{9}$$

which means that the critical drag force is $F_{Dcr} = \sqrt{F_{Grx}^2 + F_{Gry}^2}$.

Similarly, the threshold of motion for the forces normal to the bed is given by:

$$\sum F_{zr} = F_{Lr} + F_{Gzr} \geq 0 \tag{10}$$

and the critical lift force is given by $F_{Lcr} = F_{Gzr}$, recovering a standard grain force balance model. It is worth noting that the calculation of vector components $F_{Grx}, F_{Gry}, F_{Grz}$ is simplified significantly with the use of quaternions as they need

https://doi.org/10.5194/esurf-2020-20
Preprint. Discussion started: 3 April 2020

to be defined once from Equation 7 after the $R({}^r_i q)$ matrix is defined. A second important point is that the definition of the components F_{Dr} and F_{Lr} does not imply any assumptions about the direction of the motion of the particle. By tracking the orientation of the particle in relation to the r frame (often referred as *attitude*) it is possible to simply map the F_{Dr} and F_{Lr} as components of the resultant force as the balance of equation 5 is resolved.

Finally, to account for both the duration and the magnitude of a force the impulse for duration T_i starting from the time t_i is defined as:

$$\int_{t_i}^{t_i+T_i} F(t)dt \tag{11}$$

The subsequent analysis focuses on the calculation of impulses for the time durations Ti when drag and/or lift forces exceed critical thresholds (Diplas et al., 2008; Celik et al., 2010; Valyrakis et al., 2010). The term *impulse* is used here to refer to *inertial* impulses, i.e. those calculated from intertial forces that occur when the F_{Dcr} and F_{Lcr} force thresholds of motion (Equations 9 and 10) are exceeded. Those impulses are transferred to the particle from fluid turbulence and coherent flow structures, however this transfer is not described in this work. Here, the inertial impulses capture directly the flow-particle interaction and specifically the forcing that mobilises the particle.

5 Laboratory and field experiments

Two sensor assemblies were deployed, one sphere and one ellipsoid (described in Maniatis, 2016). The 90 mm diameter, 1.019 kg, sphere is solid aluminium with a symmetrical cavity for the IMU centred at the origin of the sphere. The ellipsoid (axes 100, 70, 30mm), made of the same material, weighs 0.942 kg. The cavity in the ellipsoid was designed to ensure that the IMU axes align with the principal axes of the whole device. The density of both devices after the cavity cut is 2670 ± 3 kg.m^{-3} approximating the density of quartz (2650 kg.m^{-3}). The measuring unit is the TSS-DL-HH-S sensor from Yei-Technologies^{TM} (YEI, 2014), equipped with a gyroscope ($\pm 2000°$.s^{-1} sensitivity) and an accelerometer with a maximum range of ± 400 g. The acceleration range is one of the main reasons for the selection of this IMU as lower range accelerometers (particularly those in the very common ± 20 g range) are not suitable for capturing the full range of forces in natural environments (Maniatis et al., 2013). The nominal sampling frequency of the sensor is 50 Hz which permits constant use for approximately 5 hours (LiPo rechargeable battery). The factory maximum sampling frequency is 250 Hz.

5.0.1 Laboratory entrainment experiments and separation of impulsive events

All experiments took place in a flume with a bed slope of S = 0.02 which corresponds to an orientation given by the quaternion ${}^r_i q$ = [0.92, 0.14, -20, 028]. The ${}^r_i q$ was measured by aligning the X-IMU axis with the centreline of the flume, the Y-IMU axis with the transverse direction and the Z-IMU axis with the direction normal to the bed. The positive X-IMU axis coincides with cross-section averaged flow direction. A bed of plastic hemispheres of the same diameter (90 mm) was the spherical device was constructed. The hemispheres where glued to form a 0.5 m (L) x 0.9 m (W) section. Both the hemispheres section and the upstream flume surface were roughened with 1.5 mm diameter uniform sand to increase roughness and reduce the possibility of slipping.

For the experiments, the spherical device was placed on the flume centreline in a saddle position between four bed hemispheres and the three sensor axes were aligned with the inertial frame i (${}_{i}^{b}q$ = [1,0,0,0], Appendix A). After positioning the sensor, the discharge was increased at a constant rate of 0.028 l.s^{-1} until the particle was entrained. Acceleration and rotation were measured for the duration of the flow increase, throughout the sensor movement, and for 10 further seconds after it stopped moving. All the experiments were recorded at 60 fps using a standard GoPro Hero 7. The same experimental protocol was followed for the ellipsoid device, differing only in that the particle was initially aligned to the frame of reference of the flume bed (${}_{i}^{b}q$ = ${}_{i}^{r}q$ = [0.92, 0.14, -20, 028]). This resulted in the X - sensor long axis coinciding with the X flume direction (the direction of the flow (Figure 1).

Ten entrainment experiments were conducted with each device. Drag and lift forces as well as the duration and the generated impulse during the entrainment events ($F_D > F_{Dcr}$ and/or $F_L > F_{Lcr}$) were calculated using the derivations of section 4. For the spherical sensor the deterministic drag and lift thresholds are F_{Dcr} = 3.99 N and F_{Lcr} = 7.25 N, respectively (Figure 2). The equivalent thresholds for the ellipsoid (using the geometry of a sphere of equal volume) were F_{Dcr} = 5.11 N and F_{Lcr} = 9.28 N. The hydraulic parameters for all the experiments were measured at the threshold discharge for entrainment of the spherical particle (Q= 30 ± 2 l.s^{-1}) and are summarised in Table B1.

5.0.2 Probabilistic impulse threshold for motion

Entrainment was observed independently from video recordings which were synchronised with the experiments from the start of the flow increase (Section 5.0.1). Entrainment was defined as having occurred when the sphere was displaced by one diameter, and the ellipsoid by one long-axis displacement. These visual observations are used to statistically calculate the probability of entrainment as a function of inertial impulses (Figure 4). Following the framework presented in Maniatis et al. (2017), the exact time point of entrainment was noted in the video recording and the derived inertial impulses were separated into a binary, pre- and post-entrainment, data set. A logistic regression was used to describe the probability of entrainment, with Pr > 0.5 defining the threshold of motion. Following the conceptualisation in Grass (1970), exceeding that threshold relates to impulses that are more able to dislodge the particle, in contrast to the conditions below threshold that relate more to pre-entrainment vibrations. Video recording was not possible in the field setting, so this calculation is only presented for the laboratory experiments.

5.0.3 Field testing

Field experiments took place within a 5 m long straight and confined reach of the Erlenbach mountain stream in Switzerland, approximately 15 m upstream of the concrete channel section and 55m upstream of the sediment retention basin (the position where the geo-phone sensors are installed, providing continuous bed-load transport measurements for the last 30 years (Turowski et al., 2011; Rickenmann et al., 2012). Taking advantage of the dominant step-pool morphology of the stream (areas of

https://doi.org/10.5194/esurf-2020-20
Preprint. Discussion started: 3 April 2020

Earth Surface Dynamics Discussions

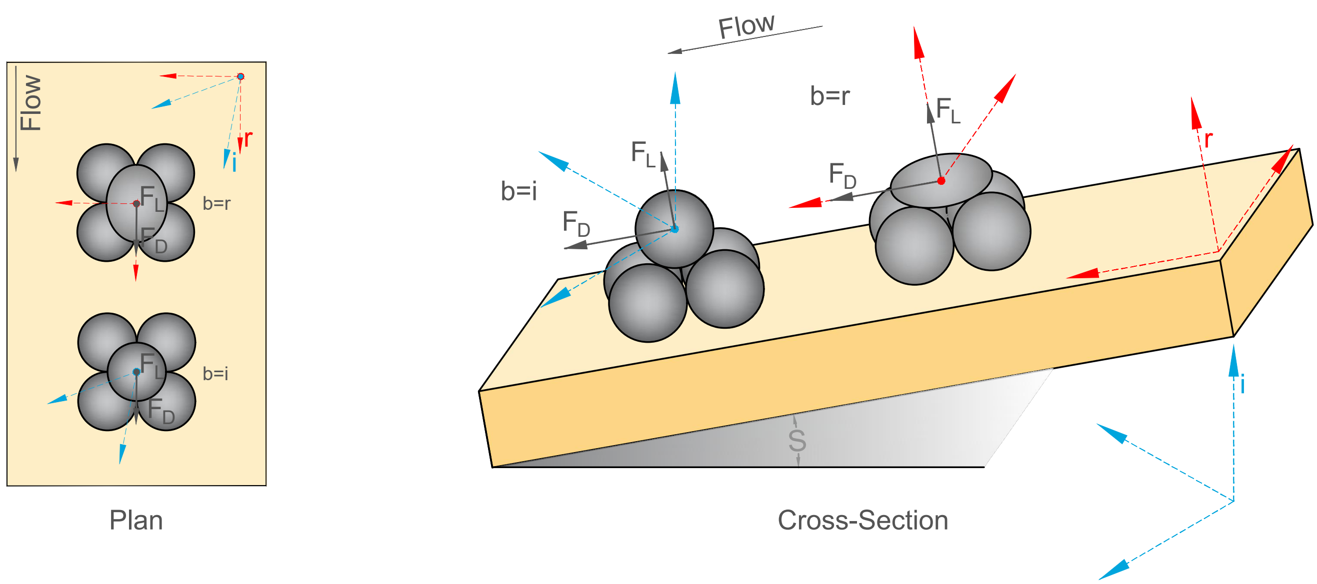

Figure 1. Initial sensor alignment for laboratory experiments r stands for river-bed (flume in this case) reference frame, b for body frame and i for the inertial reference frame. ${}^{r}_{i}q$ = [0.92, 0.14, -20, 028]. F_D and F_L and the drag and lift components of the resultant force mapped in the r frame. S is the slope of the channel (0.02)

fast flows leading to pools where the sensor can be retrieved), the ellipsoid sensor was submerged (on a step), aligned to the same orientation with the riverbed (${}^{b}_{i}q$ = ${}^{r}_{i}q$ = [0.50 -0.39 0.34 -0.68], assumed parallel to the banks and the cross-averaged flow direction, at the approximate centre line of the stream and allowed to be transported until it stopped moving and rested immobile for at least 10 seconds (Figure 2e). The first one second of each transport event was removed from the data as the effect of holding and releasing the sensor were still present. Ten transport events were recorded and processed similarly to the incipient motion experiments. The average travel distance for each transport event was 2 $\pm$0.43 m (from the point of release to the point of deposition, tape measurements) and the average event duration (after the first second of release) was 3 $\pm$0.6 seconds (Figure 2). To establish a representative orientation for the reach (in relation to the orientation of gravity), the IMU was aligned parallel to the approximate centreline (X-IMU axis, X^+ = cross-section averaged flow direction), trasverse (Y-IMU axis) and normal to the bed (Z-IMU axis) directions within the stream. The hydraulic parameters are summarised in Table B2.

6 Results

The flume experiments demonstrate the differences between the spherical and the ellipsoid particle during incipient motion (Figures 3 and 4). For the sphere, drag and lift impulses over the critical force thresholds ($F_D > F_{Dcr}$ and $F_L > F_{Lcr}$) occur

https://doi.org/10.5194/esurf-2020-20
Preprint. Discussion started: 3 April 2020

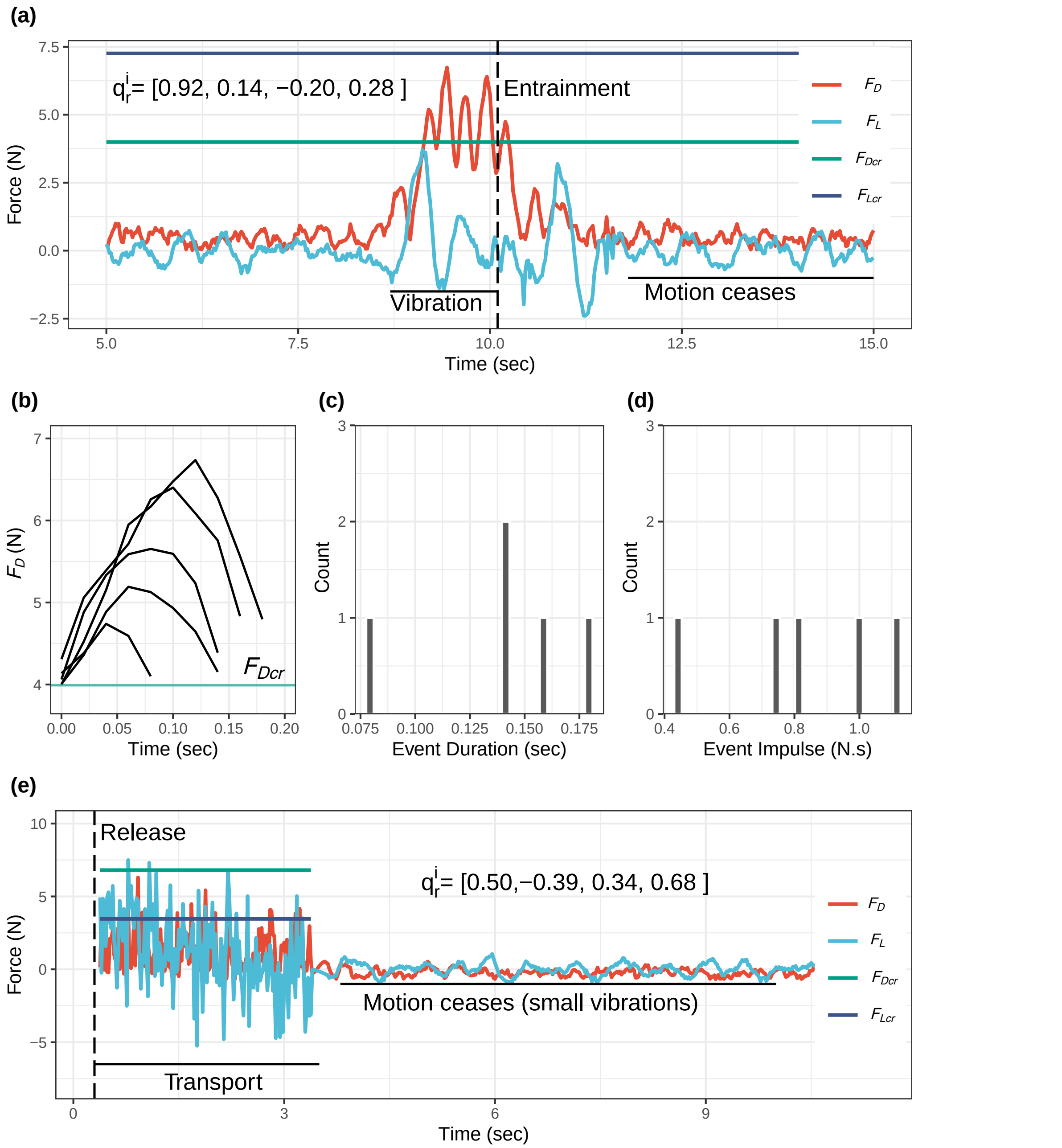

Figure 2. Example flume and field experiments (a) Calculated drag, F_D, and lift, F_L, forces. F_D (summation of inertial forces on the 2D-plane parallel to the flume bed) and F_L (inertial force recorded along the normal to the flume bed direction) for one flume experiment using the spherical sensor. The deterministic force thresholds (F_{Dcr} = 3.99 N and F_{Lcr} = 7.25 N) have been calculated using Equations 9 and 10. The vertical dashed line (t=10.1 s), shows the exact point of entrainment as determined from the video recording **(b)** Drag forces recorded during the five threshold exceedance events (where the drag force [red line] exceeds the threshold [green line] in (a)) events; **(c)** and **(d)** Duration and impulse, respectively, for the five events in (b). **(e)** is the equivalent of plot (a) for one field experiment (Erlenbach). The vertical line indicates the time of one second after the release of the sensor (see Section 5.0.3)

Earth Surface Dynamics Discussions
Open Access
EGU

for similar durations and generate impulses of similar magnitude. Differences can be observed between the right tails of the drag and lift distributions, for both durations and impulses, with the drag distributions being more skewed resulting in a higher median for the $F_D > F_{Dcr}$ events ($F_D > F_{Dcr}$ impulses median = 0.248 N.s, $F_L > F_{Lcr}$ impulses median= 0.13 N.s). The relationship between the duration of exceedance events and the generated impulse follows an approximately linear trend, although variability is higher for the relationship between drag impulses *I* and corresponding durations (*t*). For the relationship *I* vs *t*, R^2 = 0.84 (p-value $< 2.2 \text{ x } 10^{-16}$) for the drag events and 0.89 (p-value $< 4.2 \text{ x } 10^{-9}$)) for the lift events (Figure 3 (a)).

The results from the ellipsoid sensor demonstrate a strong influence of the lift forces. Exceedance impulses occur for similar durations and magnitudes, however there is a strong bias of the lift distribution towards the shorter and low impulse events. A similarity with the spherical particle is that drag duration and impulse distributions include more outliers than the lift distributions ($F_D > F_{Dcr}$ impulses median = 0.104 N.s, $F_L > F_{Lcr}$ impulses median= 0.022 N.s). The relationship between the duration of exceedance events and the generated impulse is less linear than for the sphere. For the ellipsoid, the *I* vs t relationship has R^2 = 0.79 (p-value $< 2.2 \text{ x } 10^{-16}$) for the drag events and 0.67 (p-value $< 2.2 \text{ x } 10^{-16}$) for the lift events (Figure 3 (b)). For all these threshold exceeding events the sensor was vibrating until entrained (observed from both video and IMU data).

Using the video recording observations, the thresholds for entrainment were approximated with a logistic regression. The probability of entrainment as a function of impulse (Figure 4 (a) and (b)) highlights the control of short lift events on the entrainment of the ellipsoid. The impulse threshold for the sphere is close to 0, as all the approximated probabilities exceed 0.5. However, there is significant variability in this calculation (wide 95% confidence intervals) which is indicative of the random fluctuation of impulse in relation to entrainment events for the sphere. In contrast, the entrainment of the ellipsoid demonstrates an observable dependency on lift impulses as the lift threshold is lower (ellipsoid lift impulse threshold = 0.27 $\pm$ 0.03 N.s) and the drag threshold is approximated with less confidence (ellipsoid drag impulse threshold = 1.26 $\pm$ 0.23 N.s).

Finally, the results from the field experiments (Figure 5) show the scale difference between the flume and the natural environment. Drag forces are of higher magnitude and duration than the lift forces ($F_D > F_{Dcr}$ impulses mean = 0.96 N.s, $F_L > F_{Lcr}$ impulses mean= 0.13 N.s), but there is an abundance of low magnitude lift impulses that affect strongly the motion of the ellipsoid. Both drag and lift distributions are heavy tailed ($F_D > F_{Dcr}$ impulses median = 0.7 N.s, $F_L > F_{Lcr}$ impulses median= 0.071 N.s., skewness equal to 1.82 and 6.84, respectively). Indicative of the rapidity of motion in the natural stream is the linearity of the *I* vs *t* relationship. While in the laboratory experiments the gradual increase of the flow let the ellipsoid respond in various ways to the turbulent structures (Table B2), in the Erlenbach the duration of the exceedence events is a direct proxy for the generated impulse (*I* vs t R^2 = 0.967 (p-value $< 2.2 \text{ x } 10^{-16}$) for the drag events and 0.884 (p-value $< 2.2 \text{ x } 10^{-16}$) for the lift events).

https://doi.org/10.5194/esurf-2020-20
Preprint. Discussion started: 3 April 2020

Earth Surface Dynamics Discussions
Open Access

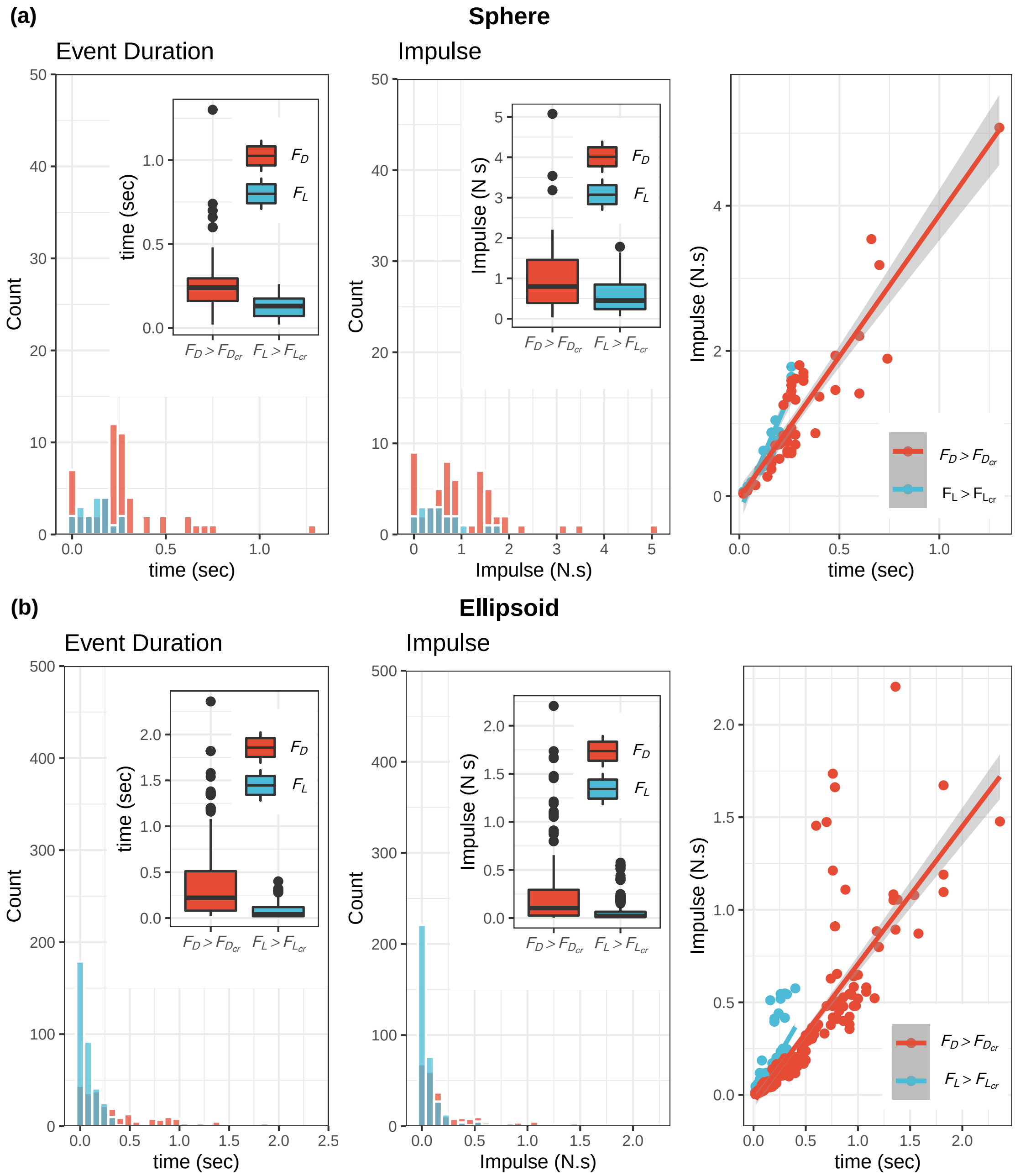

Figure 3. Inertial impulses and duration of threshold exceedance events for laboratory experiments. For the spherical particle **(a)** the drag inertial impulse median (median of $F_D > F_{Dcr}$ events) is 0.118 N.s higher than the lift inertia impulse median (median of $F_L > F_{Lcr}$ events). For the ellipsoid **(b)** the equivalent difference is 0.082 N.s. The relationship between the duration (t) and the inertial impulse (I) during the exceedence events is linear for both the sphere and the ellispoid (and for both $F_D > F_{Dcr}$ and $F_L > F_{Lcr}$) events. The entrainment of the ellipsoid is more dependent on short and low lift inertial impulses (and has more variable I vs t relationship) than the sphere, demonstrating the effect of shape on the inertial dynamics.

https://doi.org/10.5194/esurf-2020-20
Preprint. Discussion started: 3 April 2020

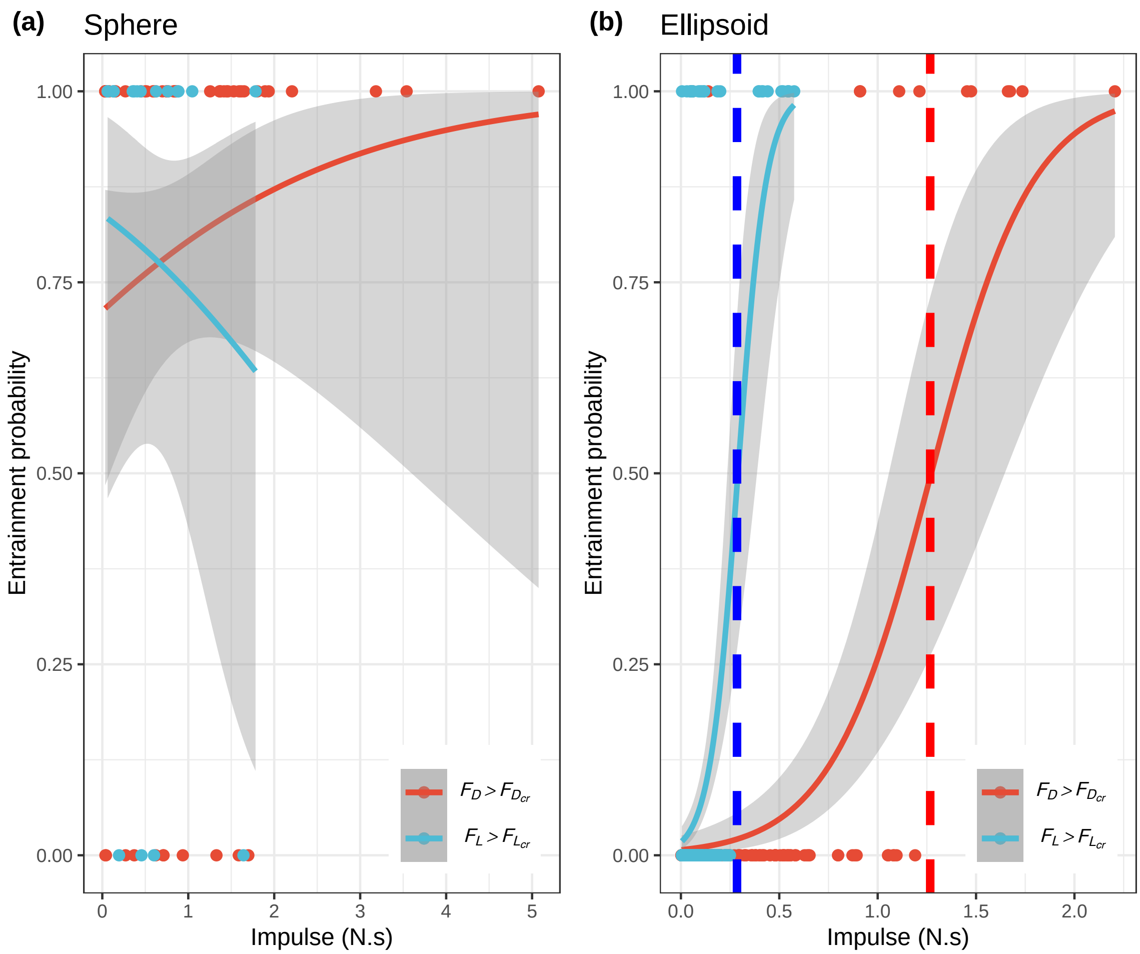

Figure 4. Probabilistic inertial impulse threshold for laboratory experiments. Logistic regression of the probability of entrainment for the spherical **(a)** and ellipsoid **(b)** particles. The calculation is based on the combination of video recordings and inertial impulse measurements during drag and lift threshold exceedance ($F_D > F_{Dcr}$ and $F_L > F_{Lcr}$ events). For the sphere there is little statistical difference between the calculated inertial impulses as over 95 % of the values relate to an entrainment event (the probability threshold 0.5 is always exceeded). For the ellipsoid, the probabilistic lift inertial impulse threshold relaxes to 0.27 N.s (blue vertical line, (b)) and the drag threshold relaxes to 1.26 N.s (red vertical line, (b)).

https://doi.org/10.5194/esurf-2020-20
Preprint. Discussion started: 3 April 2020

Earth Surface Dynamics Discussions

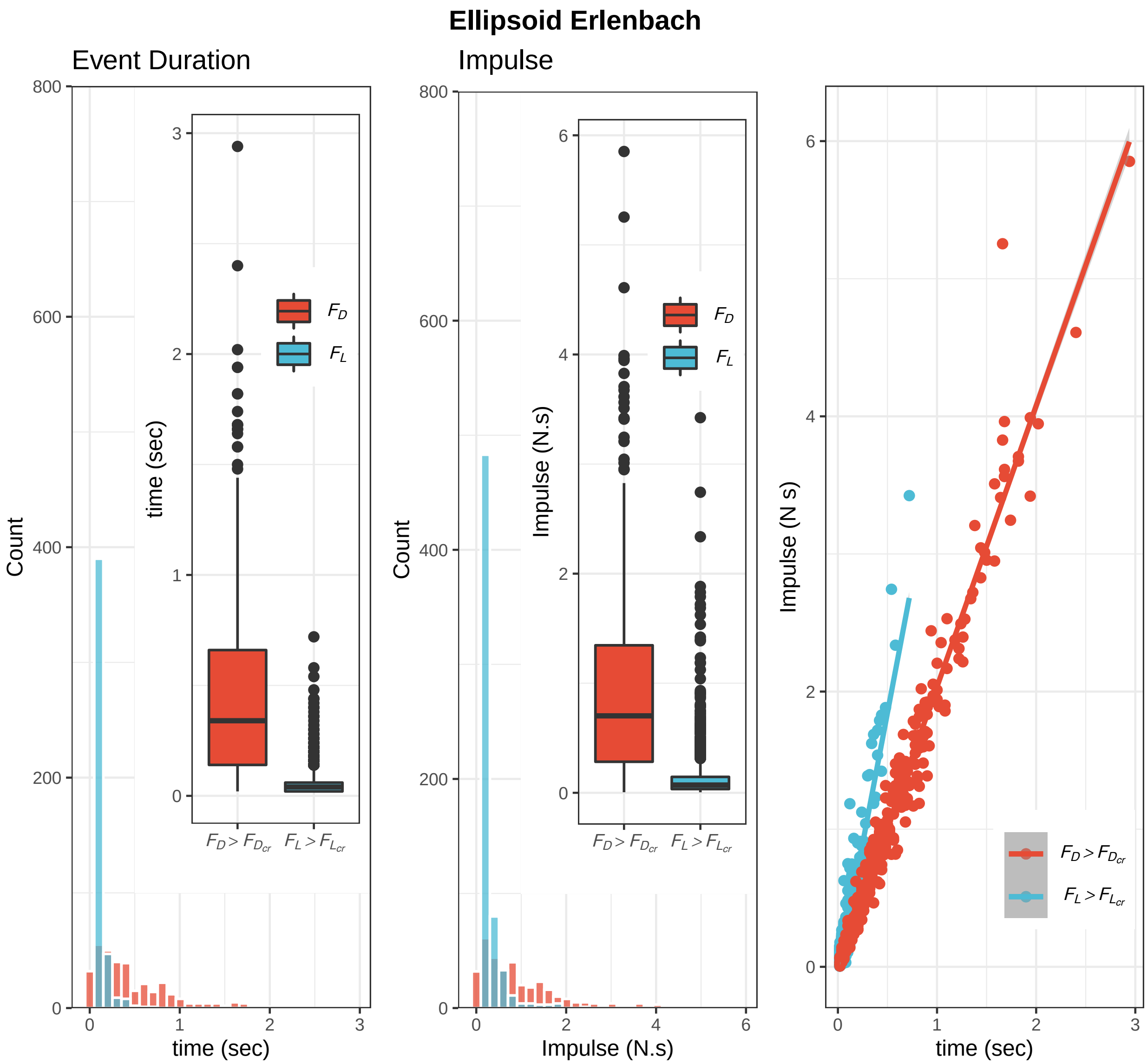

Figure 5. Inertial Impulses and duration of threshold exceedance events for field experiments. During short transport events (average travel distance = 2 ±0.43 m) the drag inertial impulse median (median of $F_D > F_{Dcr}$ events) is 0.62 N.s higher than the lift inertia impulse median (median of $F_L > F_{Lcr}$ events). The relationship between the duration (t) and the inertial impulse (I) is linear for both for both $F_D > F_{Dcr}$ and $F_L > F_{Lcr}$ events. During *in-situ* transport the drag forces are of higher magnitude and duration, however, short and low magnitude $F_L > F_{Lcr}$ impulses have a strong influence on the motion of the ellipsoid.

https://doi.org/10.5194/esurf-2020-20
Preprint. Discussion started: 3 April 2020

7 Discussion

Previous laboratory studies using fixed vibration sensors attached to grains (Schmeeckle et al., 2007; Cameron et al., 2019) report *nominal* drag and lift forces at the order of magnitude of 0.1 N for 0.008 - 0.025 m diameter particles (and for comparable hydraulic conditions to the flume experiments presented here, Appendix B). In the flume results presented here, the inertial drag and lift forces during entrainment are recorded at an order of magnitude of 10 N. This two order of magnitude difference is expected since: a) the particles examined here have a 5x larger (actual or equivalent) average diameter compared to these works, resulting to a mass larger by a factor of 125; and b) the inertial sensor is unrestricted (freely mobile) meaning that the inertia of the moving particle is fully captured.

Static vibration sensors were also deployed by Lamb et al. (2017) who attached them to a wide range of test particles (cross-stream $D=$ between 0.075 and 0.218 m). The hydraulic regime they captured is directly relevant to both the laboratory and the field experiments presented here (order of magnitude of hydraulic drag forces from 10 to 100 N and 10 N for hydraulic lift forces). Thus, the magnitudes of forces recorded by Lamb et al. (2017) are consistent with the inertial forces calculated here, both studies using similar gradients and grain sizes. However, it is important to consider the type of sensor (static or restricted vs mobile), the data processing model and the experimental protocol (especially the difference between increasing vs steady flow) when different force measurements are compared.

For example, a particular focus of Lamb et al. (2017) is the observation of predominant negative lift forces (especially for partially submerged particles) that have significant morphological implications as they can potentially explain the lower sediment fluxes observed in steep mountainous streams, in addition to other reductions of turbulence intensities. In this work, the inertial negative lift forces are measured (Appendix C) but the exceedance events ($F_L > F_{Lcr}$) are only calculated for the positive lift forces. This happens because the deterministic threshold (F_{Lcr}, practically the submerged component of gravity rotated to the r frame) is positive for both the laboratory and the field experiments, resulting in the exceedances being positive. The inertial negative lift forces are components of the resultant force which can have a strong hydraulic component (as argued in Lamb et al., 2017) but they can also be a reaction to positive lift forces during the motion of the particle (and especially the motion of the ellipsoid, Figures 2 and C) which requires further investigation.

The laboratory inertial impulse calculations demonstrate that, for unrestricted entrainments, there are observable differences between spherical and ellipsoid particles with the latter being more sensitive to the lift forces at entrainment threshold conditions. Those differences can relate to previous results on selective entrainment and specifically the effect of shape on the response of particles in various hydraulic regimes (e.g. Komar and Li, 1986; Demir, 2000) and the on the mode of near-bed transport. This type of observations can now be made directly using inertial sensors.

The corresponding inertial impulse calculations from the field also demonstrate that the ellipsoid is highly sensitive to low magnitude and duration lift impulses (despite the drag forces being more persistent). In addition, we observe an increase in the negative lift forces (in comparison to the laboratory experiments, Figure C1) which can support further the assumption that the particle during transport has a directionally opposite reaction to the positive lift impulses and particularly to those that exceed the threshold. However, the relationship between the duration of the exceedance events and the corresponding impulses

https://doi.org/10.5194/esurf-2020-20
Preprint. Discussion started: 3 April 2020

is significantly more linear than the laboratory experiments. The latter requires further investigation as it can relate to previous observations of transitions from hydraulic “impulse controlled" transport (corresponding to the laboratory results presented here) to “force-magnitude controlled" transport (fully developed flow, corresponding to the dynamics recorded in Erlenbach) as described in Shih and Diplas (2018).

Overall, differences of particle inertial dynamics (such as forces and impulses) during different modes of transport (entrainment vs translation in this paper) are important because they can potentially enhance predictions for grain particle travel distances with measurements from the field and particularly for large distances (Hassan et al., 1991, 2013). Measuring those differences is the most direct insight we can have for studying the effect of several morphological controls (eg. degree of clustering, burial depths, sediment sorting) until the high-frequency 3D measurement of tracer positions during transport becomes possible.

In this paper, rotation is defined as part of the Newton-Euler model in Section 3 and the rotational component is introduced in the formula for kinetic energy. However, neither of those definitions were used in the subsequent analysis because this would require a complex analysis of error propagation during signal integration (see Introduction), a topic that needs to be resolved separately. There are also testable assumptions that require further investigation from a practical sediment-hydraulics point of view. For example, a component of the differences between laboratory and field experiments (Figures 3 and 5) can relate to the scales of turbulence (Coleman and Nikora, 2008), but testing requires detailed flow measurements that were not made during the presented experiments (eg. PIV measurements).

7.1 Extended analysis

To refine the lift and drag impulses responsible for entrainment, a bootstrap method was used. Considerable effort has previously been applied to define distributions for hydraulic impulses during the entrainment of spherical particles and relating them to critical thresholds (Diplas et al., 2008; Valyrakis et al., 2010; Celik et al., 2010; Valyrakis et al., 2010, 2011). In addition, there are recent efforts towards upscaling the effect of hydraulic impulses to fully developed bed-load equations (Shih and Diplas, 2018) and results pointing towards evaluating the morphological impact of different hydraulic impulse regimes (Phillips et al., 2018), highlighting the importance of deriving general statistical descriptions for grain inertial impulses.

Here we provide a first order generalisation for inertial impulses, by approximating the distributions of inertial lift and drag impulses for an ellipsoid particle and from a combination of of laboratory and field measurements. It is also the first step towards calculating the combined behaviour of the drag and lift distributions; a development that can lead to the definition of joint distributions that have stronger explanatory and perhaps predictive value. For the bootstrap calculations to be consistent, it is important to assume no autocorrelation between the rotated inertial drag and lift forces (F_{Dr} and F_{Lr}) as verified in Figure C2.

To combine the results from the two sets of experiments (the laboratory and field experiments using the ellipsoid) it is necessary to normalise the impulsive exceedance events since the scaling is different for the laboratory and the natural conditions. For this calculation, the normalisation is performed using the mean impulse for all the drag and positive lift impulses respectively (separately for the laboratory and field experiments, $\hat{I} = I/\bar{I}exp$). After the normalisation, the laboratory and field

https://doi.org/10.5194/esurf-2020-20
Preprint. Discussion started: 3 April 2020

results are combined into one extensive dataset of normalised drag ($\hat{I}_{Drag}$) and normalised lift ($\hat{I}_{Lift}$) impulses. The Cullen - Frey diagrams (Cullen et al., 1999, D2) indicate that three types of right tail distributions are good fitting candidates for both $\hat{I}_{Drag}$ and $\hat{I}_{Lift}$: the Weibull, the gamma and the lognormal distributions. Goodness- of- fit analysis (Table D1), shows that $\hat{I}_{Drag}$ is approximated better by a Weibull distribution (median shape = 0.85, median scale = 0.9) and the $\hat{I}_{Lift}$ is approximated better by a lognormal distribution (median meanlog = - 0.66, median sdlog = 1.13). All the statistics for the selection and the stability of the selected distributions are included in Appendix D.

The fitting of the representative distributions for $\hat{I}_{Drag}$ and $\hat{I}_{Lift}$, permits bootstrap sampling from those distributions. Figure 6 shows 50000 random $\hat{I}_{Drag}$ and $\hat{I}_{Lift}$ combinations, sampled from the selected distributions. After taking into account the normalised drag and lift impulse thresholds as defined in the Results (Figure 4), we conclude that the probability for the exceedance of the lift threshold is approximately 0.02, the probability for the exceedance of the drag threshold is approximately 0.005 and the probability of both thresholds being exceeded simultaneously is negligible (4x10^{-5}). The calculation confirms the observation that the transport of the ellipsoid particle is defined by states of no-mobility (98% for the calculated combinations corresponds to dynamics that are below the normalised probabilistic impulse threshold for entrainment, Figure 4). 79.2% of the 1146 threshold exceedance events corresponds to lift threshold exceedances, 20.2% to drag threshold exceedances and 0.4% to exceedances of both thresholds. The calculation suggests that the majority of the mobility states of the ellipsoid will relate to the action of lift forces. The very small probability for the simultaneous exceedance of both thresholds is another possible effect of the particle's shape as spherical particles will protrude more and are more likely to be equally affected by both drag and lift components (Figure 4a). This type of calculations requires sample sizes that only advanced instrumentation, such as that presented in this work, can deliver. Similar frameworks can be used for meta analysis of existing results and to inform the design of future experiments and field.

8 Conclusions

- The derivation of inertial measurements from mobile sediment grains requires a physical model that links the inertial dynamics with existing force (or moments) balance equations for sediment transport (Sections 2 and 3).

- Field and laboratory measurements of inertial lift and drag impulses highlight the different entrainment behaviours of a spherical and an ellipsoidal particle. The lift inertial force is dominant during the unrestricted entrainment of the ellipsoid while there is no statistical difference between the effects of lift and drag inertial impulses on the entrainment of the sphere (Figures 3 and 4). However, the ellipsoid is clearly dominated by the drag component during transport (Erlenbach, Figure 5).

- The type of sensors currently deployed for the measurements of grain inertial dynamics (and the associated "smart pebble" assemblies) are not suitable for tracking the position of grains (3D or even 2D). However, it is possible to measure inertial forces (and impulses) if the transformations of Section 2 are applied consistently.

https://doi.org/10.5194/esurf-2020-20
Preprint. Discussion started: 3 April 2020

Earth Surface Dynamics Discussions

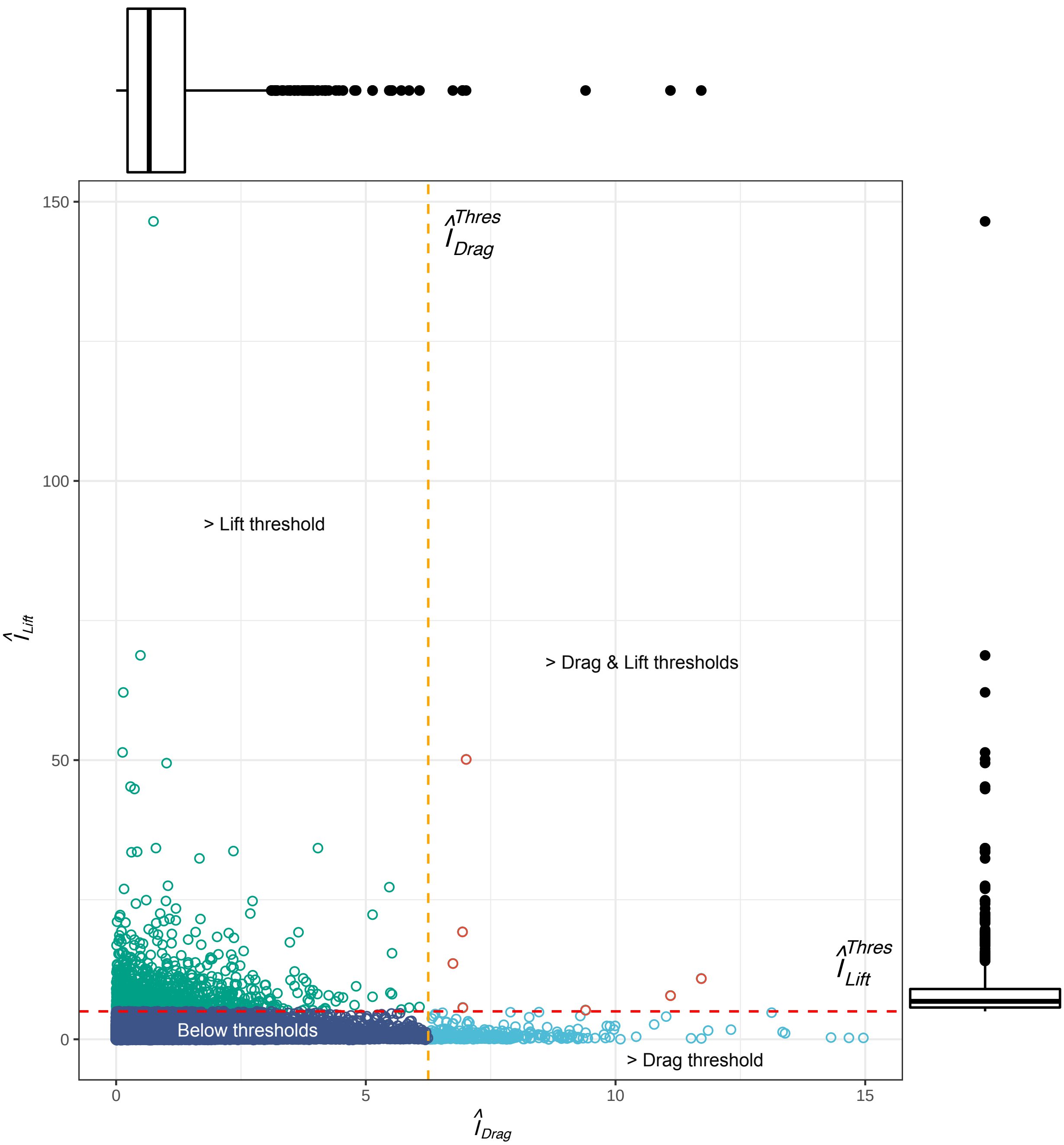

Figure 6. Bootstrap normalised impulse sampling (lift and drag). $\hat{I}_{Drag}$ and $\hat{I}_{Lift}$ are fitted with a Weibull and a log-normal distribution, respectively (Appendix D2, boxplots). The normalised drag and lift thresholds (red dashed lines), are calculated using the probabilistic drag and lift inertial impulse thresholds presented in Figure 4 which were divided by the mean inertial drag and lift impulse recorded during the laboratory experiments

https://doi.org/10.5194/esurf-2020-20
Preprint. Discussion started: 3 April 2020

– The continuous improvement of the sensor technology along with the better understanding of the physics described by inertial measurements can lead to a unified treatment of the resultant grain dynamics during bed-load transport. These are the dynamics that represent exactly the interaction of hydraulic (turbulence) and sediment forces in different regimes and can enhance the parametrisation of important hydro-morphological controls.

https://doi.org/10.5194/esurf-2020-20
Preprint. Discussion started: 3 April 2020

References

Akeila, E., Salcic, Z., and Swain, A.: Smart pebble for monitoring riverbed sediment transport, Sensors Journal, IEEE, 10, 1705–1717, 2010.

Ali, S. Z. and Dey, S.: Hydrodynamics of sediment threshold, Physics of Fluids, 28, 075 103, 2016.

Ancey, C., Davison, A., Böhm, T., Jodeau, M., and Frey, P.: Entrainment and motion of coarse particles in a shallow water stream down a steep slope, Journal of Fluid Mechanics, 595, 83–114, 2008.

Ashida, K. and Michiue, M.: An investigation of river bed degradation downstream of a dam, in: in Proceedings of 14th Int. Association of Hydraulic Research Congress, vol. 3, pp. 247–255, Wallingford, U.K., 1971.

Bialik, R. J., Nikora, V. I., Karpiński, M., and Rowiński, P. M.: Diffusion of bedload particles in open-channel flows: distribution of travel times and second-order statistics of particle trajectories, Environmental Fluid Mechanics, 15, 1281–1292, 2015.

Buffington, J. M. and Montgomery, D. R.: A systematic analysis of eight decades of incipient motion studies, with special reference to gravel-bedded rivers, Water Resources Research, 33, 1993–2029, 1997.

Buffington, J. M., Dietrich, W. E., and Kirchner, J. W.: Friction angle measurements on a naturally formed gravel streambed: implications for critical boundary shear stress, Water Resources Research, 28, 411–425, 1992.

Burtin, A., Hovius, N., McArdell, B., Turowski, J., and Vergne, J.: Seismic constraints on dynamic links between geomorphic processes and routing of sediment in a steep mountain catchment, Earth Surface Dynamics, 2, 21–33, 2014.

Cameron, S., Nikora, V., and Marusic, I.: Drag forces on a bed particle in open-channel flow: Effects of pressure spatial fluctuations and very-large-scale motions, Journal of Fluid Mechanics, 863, 494–512, 2019.

Celik, A. O., Diplas, P., Dancey, C. L., and Valyrakis, M.: Impulse and particle dislodgement under turbulent flow conditions, Physics of Fluids, 22, 046 601, 2010.

Coleman, S. and Nikora, V.: A unifying framework for particle entrainment, Water resources research, 44, 2008.

Constantinescu, G., Garcia, M., and Hanes, D.: River Flow 2016: Iowa City, USA, July 11-14, 2016, Crc Press, 2016.

Cullen, A. C., Frey, H. C., and Frey, C. H.: Probabilistic techniques in exposure assessment: a handbook for dealing with variability and uncertainty in models and inputs, Springer Science & Business Media, 1999.

Delignette-Muller, M. L., Dutang, C., et al.: fitdistrplus: An R package for fitting distributions, Journal of statistical software, 64, 1–34, 2015.

Demir, T.: The influence of particle shape on bedload transport in coarse-bed river channels, Ph.D. thesis, Durham University, 2000.

Dey, S.: Sediment threshold, Applied Mathematical Modelling, 23, 399–417, 1999.

Dey, S. and Ali, S. Z.: Advances in modeling of bed particle entrainment sheared by turbulent flow, Physics of Fluids, 30, 061 301, 2018.

Diebel, J.: Representing attitude: Euler angles, unit quaternions, and rotation vectors, Matrix, 58, 1–35, 2006.

Diplas, P., Dancey, C. L., Celik, A. O., Valyrakis, M., Greer, K., and Akar, T.: The role of impulse on the initiation of particle movement under turbulent flow conditions, Science, 322, 717–720, 2008.

Einstein, H. A.: Bedload Transport as a Probability Problem, Mitteilung der Versuchsanstalt für Wasserbau an der EidgenÃssischen Technischen Hochschule, p. 110, 1937.

Ergenzinger, P. and Jupner, R.: Using COSSY (CObble Satellite SYstem) for measuring the effects of lift and drag forces, Erosion and Sediment Transport Monitoring Programmes in river Basins, IAHS Publi, 41–50, 1992.

Fathel, S., Furbish, D., and Schmeeckle, M.: Parsing anomalous versus normal diffusive behavior of bed load sediment particles, Earth Surface Processes and Landforms, 2016.

https://doi.org/10.5194/esurf-2020-20
Preprint. Discussion started: 3 April 2020

Ferguson, R. I., Bloomer, D. J., Hoey, T. B., and Werritty, A.: Mobility of river tracer pebbles over different timescales, Water Resources Research, 38, 3–1, 2002.

Frank, D., Foster, D., Sou, I. M., Calantoni, J., and Chou, P.: Lagrangian measurements of incipient motion in oscillatory flows, Journal of Geophysical Research: Oceans, 120, 244–256, 2015.

Gebre-Egziabher, D., Hayward, R. C., and Powell, J. D.: A low-cost GPS/inertial attitude heading reference system (AHRS) for general aviation applications, in: Position Location and Navigation Symposium, IEEE 1998, pp. 518–525, IEEE, 1998.

Gilbert, G. K. and Murphy, E. C.: The transportation of debris by running water, 86, US Government Printing Office, 1914.

Gimbert, F., Fuller, B. M., Lamb, M. P., Tsai, V. C., and Johnson, J. P.: Particle transport mechanics and induced seismic noise in steep flume experiments with accelerometer-embedded tracers, Earth Surface Processes and Landforms, 2019.

Grass, A. J.: Initial instability of fine bed sand, Journal of the Hydraulics Division, 96, 619–632, 1970.

Grewal, M. S., Weill, L. R., and Andrews, A. P.: Global positioning systems, inertial navigation, and integration, John Wiley & Sons, 2007.

Gronz, O., Hiller, P. H., Wirtz, S., Becker, K., Iserloh, T., Seeger, M., Brings, C., Aberle, J., Casper, M. C., and Ries, J. B.: Smartstones: A small 9-axis sensor implanted in stones to track their movements, Catena, 142, 245–251, 2016.

Hamilton, W. R.: Ii. on quaternions; or on a new system of imaginaries in algebra, The London, Edinburgh, and Dublin Philosophical Magazine and Journal of Science, 25, 10–13, 1844.

Hassan, M. A. and Roy, A. G.: Coarse particle tracing in fluvial geomorphology, Tools in Fluvial Geomorphology, pp. 306–323, 2016.

Hassan, M. A., Church, M., and Schick, A. P.: Distance of movement of coarse particles in gravel bed streams, Water Resources Research, 27, 503–511, 1991.

Hassan, M. A., Church, M., and Ashworth, P. J.: Virtual rate and mean distance of travel of individual clasts in gravel-bed channels, Earth Surface Processes and Landforms, 17, 617–627, 1992.

Hassan, M. A., Church, M., Rempel, J., and Enkin, R. J.: Promise, performance and current limitations of a magnetic Bedload Movement Detector, Earth Surface Processes and Landforms, 34, 1022–1032, 2009.

Hassan, M. A., Voepel, H., Schumer, R., Parker, G., and Fraccarollo, L.: Displacement characteristics of coarse fluvial bed sediment, Journal of Geophysical Research: Earth Surface, 118, 155–165, 2013.

Hodge, R. A., Hoey, T. B., and Sklar, L. S.: Bed load transport in bedrock rivers: the role of sediment cover in grain entrainment, translation, and deposition, Journal of Geophysical Research, 116, 1–19, https://doi.org/10.1029/2011JF002032, http://www.agu.org/pubs/crossref/2011/2011JF002032.shtml, 2011.

Hodge, R. A., Sear, D. A., and Leyland, J.: Spatial variations in surface sediment structure in riffle–pool sequences: a preliminary test of the Differential Sediment Entrainment Hypothesis (DSEH), Earth surface processes and landforms, 38, 449–465, 2013.

Ikeda, S.: Incipient motion of sand particles on side slopes, Journal of the Hydraulics Division, 108, 95–114, 1982.

Iwagaki, Y.: Basic studies on the critical tractive force (1), Transactions of the JSCE, 31, 1–20, 1956.

Johnson, J. P.: Gravel threshold of motion: a state function of sediment transport disequilibrium?, Earth Surface Dynamics, 4, 685–703, 2016.

Johnson, M. F., Rice, S. P., and Reid, I.: Increase in coarse sediment transport associated with disturbance of gravel river beds by signal crayfish (*Pacifastacus Leniusculus*), Earth Surface Processes and Landforms, 36, 1680–1692, https://doi.org/10.1002/esp.2192, http://dx.doi.org/10.1002/esp.2192, 2011.

Kirchner, J. W., Dietrich, W. E., Iseya, F., and Ikeda, H.: The variability of critical shear stress, friction angle, and grain protrusion in water-worked sediments, Sedimentology, 37, 647–672, https://doi.org/10.1111/j.1365-3091.1990.tb00627.x., 1990.

https://doi.org/10.5194/esurf-2020-20
Preprint. Discussion started: 3 April 2020

Kline, S., Reynolds, W., Schraub, F., and Runstadler, P.: The structure of turbulent boundary layers, Journal of Fluid Mechanics, 30, 741–773, https://doi.org/10.1017/S0022112067001740, 1967.

Kok, M., Hol, J. D., and Schön, T. B.: Using inertial sensors for position and orientation estimation, arXiv preprint arXiv:1704.06053, 2017.

Komar, P. D. and Li, Z.: Pivoting analyses of the selective entrainment of sediments by shape and size with application to gravel threshold, Sedimentology, 33, 425–436, 1986.

Komar, P. D. and Li, Z.: Applications of grain-pivoting and sliding analyses to selective entrapment of gravel and to flow-competence evaluations, Sedimentology, 35, 681–695, 1988.

Kularatna, N., Melville, B., Akeila, E., and Kularatna, D.: Implementation aspects and offline digital signal processing of a smart pebble for river bed sediment transport monitoring, in: Sensors, 2006. 5th IEEE Conference on, pp. 1093–1098, IEEE, 2006.

Lamb, M. P., Brun, F., and Fuller, B. M.: Direct measurements of lift and drag on shallowly submerged cobbles in steep streams: Implications for flow resistance and sediment transport, Water Resources Research, 53, 7607–7629, 2017.

Liedermann, M., Tritthart, M., and Habersack, H.: Particle path characteristics at the large gravel-bed river Danube : results from a tracer study and numerical modelling, Earth Surface Processes and Landforms, 38, 512–522, https://doi.org/10.1002/esp.3338, 2012.

Maniatis, G.: Eulerian-Lagrangian definition of coarse bed-load transport: theory and verification with low-cost inertial measurement units, Ph.D. thesis, University of Glasgow, 2016.

Maniatis, G., Hoey, T., and Sventek, J.: Sensor Enclosures: Example Application and Implications for Data Coherence, Journal of Sensor and Actuator Networks, 2, 761, 2013.

Maniatis, G., Hoey, T. B., Hassan, M. A., Sventek, J., Hodge, R., Drysdale, T., and Valyrakis, M.: Calculating the explicit probability of entrainment based on inertial acceleration measurements, Journal of Hydraulic Engineering, 143, 2017.

Marion, A. and Tregnaghi, M.: A new theoretical framework to model incipient motion of sediment grains and implications for the use of modern experimental techniques, in: Experimental and Computational Solutions of Hydraulic Problems, pp. 85–100, Springer, 2013.

Masteller, C. C., Finnegan, N. J., Turowski, J. M., Yager, E. M., and Rickenmann, D.: History-Dependent Threshold for Motion Revealed by Continuous Bedload Transport Measurements in a Steep Mountain Stream, Geophysical Research Letters, 46, 2583–2591, 2019.

McEwan, I., Habersack, H., and Heald, J.: Discrete particle modelling and active tracers: new techniques for studying sediment transport as a Lagrangian phenomenon, Gravel bed rivers V (ed. MP Mosley), pp. 339–360, 2001.

McEwan, I., Sørensen, M., Heald, J., Tait, S., Cunningham, G., Goring, D., and Willetts, B.: Probabilistic modeling of bed-load composition, Journal of Hydraulic Engineering, 130, 129–139, 2004.

Murdoch, D. and Murdoch, M. D.: Package 'orientlib', 2015.

Nelson, J. M., Shreve, R. L., McLean, S. R., and Drake, T. G.: Role of near-bed turbulence structure in bed load transport and bed form mechanics, Water Resources Research, 31, 2071–2086, https://doi.org/10.1029/ 95WR00976, 1995.

Niño, Y. and García, M.: Using Lagrangian particle saltation observations for bedload sediment transport modelling, Hydrological Processes, 12, 1197–1218, 1998.

Olinde, L. and Johnson, J. P.: Using RFID and accelerometer-embedded tracers to measure probabilities of bed load transport, step lengths, and rest times in a mountain stream, Water Resources Research, 51, 7572–7589, 2015.

O'Reilly, O. M.: Intermediate dynamics for engineers: a unified treatment of Newton-Euler and Lagrangian mechanics, AMC, 10, 12, 2008.

Papanicolaou, A., Diplas, P., Evaggelopoulos, N., and Fotopoulos, S.: Stochastic incipient motion criterion for spheres under various bed packing conditions, Journal of Hydraulic Engineering, 128, 369–380, 2002.

Phillips, C., Hill, K. M., Paola, C., Singer, M., and Jerolmack, D.: Effect of flood hydrograph duration, magnitude, and shape on bed load transport dynamics, Geophysical Research Letters, 45, 8264–8271, 2018.

Prancevic, J. P. and Lamb, M. P.: Particle friction angles in steep mountain channels, Journal of Geophysical Research: Earth Surface, 120, 242–259, 2015.

Recking, A., Piton, G., Vazquez-Tarrio, D., and Parker, G.: Quantifying the morphological print of bedload transport, Earth Surface Processes and Landforms, 2015.

Rickenmann, D., Turowski, J. M., Fritschi, B., Klaiber, A., and Ludwig, A.: Bedload transport measurements at the Erlenbach stream with geophones and automated basket samplers, Earth Surface Processes and Landforms, 37, 1000–1011, 2012.

Schmeeckle, M. W., Nelson, J. M., and Shreve, R. L.: Forces on stationary particles in near-bed turbulent flows, Journal of Geophysical Research: Earth Surface (2003–2012), 112, https://doi.org/10.1029/2006JF000536, 2007.

Schmidt, K.-H. and Ergenzinger, P.: Bedload entrainment, travel lengths, step lengths, rest periods—studied with passive (iron, magnetic) and active (radio) tracer techniques, Earth Surface Processes and Landforms, 17, 147–165, 1992.

Schneider, J. M., Turowski, J. M., Rickenmann, D., Hegglin, R., Arrigo, S., Mao, L., and Kirchner, J. W.: Scaling relationships between bed load volumes, transport distances, and stream power in steep mountain channels, Journal of Geophysical Research: Earth Surface, 119, 533–549, 2014.

Shields, A.: Application of similarity principles and turbulence research to bed-load movement, Technical Report, Soil Conservation Service, 1936.

Shih, W. and Diplas, P.: A unified approach to bed load transport description over a wide range of flow conditions via the use of conditional data treatment, Water Resources Research, 54, 3490–3509, 2018.

Shvidchenko, A. B. and Pender, G.: Flume study of the effect of relative depth on the incipient motion of coarse uniform sediments, Water Resources Research, 36, 619–628, 2000.

Spazzapan, M., Petrovčič, J., and Mikoš, M.: New tracer for monitoring dynamics of sediment transport in turbulent flows, Acta Hydrotechnica, 22, 135–148, 2004.

Tsakiris, A. G., Papanicolaou, A., Moustakidis, I., and Abban, B. K.: Identification of the Burial Depth of Radio Frequency Identification Transponders in Riverine Applications, Journal of Hydraulic Engineering, 141, 04015 007, 2015.

Tucker, G. E. and Hancock, G. R.: Modelling landscape evolution, Earth Surface Processes and Landforms, 35, 28–50, 2010.

Turowski, J. M., Badoux, A., and Rickenmann, D.: Start and end of bedload transport in gravel-bed streams, Geophysical Research Letters, 38, 2011.

Valenti, R. G., Dryanovski, I., and Xiao, J.: Keeping a good attitude: A quaternion-based orientation filter for IMUs and MARGs, Sensors, 15, 19 302–19 330, 2015.

Valyrakis, M., Diplas, P., Dancey, C. L., Greer, K., and Celik, A. O.: Role of instantaneous force magnitude and duration on particle entrainment, Journal of Geophysical Research: Earth Surface (2003–2012), 115, 2010.

Valyrakis, M., Diplas, P., and Dancey, C. L.: Entrainment of coarse grains in turbulent flows: An extreme value theory approach, Water Resources Research, 47, 2011.

Van Rijn, L. C.: Sediment transport, part I: bed load transport, Journal of Hydraulic Engineering, 110, 1431–1456, 1984.

VectorNav: Inertial Measurement Units and Inertial Navigation, VecotrNav webpage: www.vectornav.com/support/library/imu-and-ins, Accessed 2016-05-09, 2016.

Vignaga, E., Sloan, D. M., Luo, X., Haynes, H., Phoenix, V. R., and Sloan, W. T.: Erosion of biofilm-bound fluvial sediments, Nature Geoscience, 6, 770–774, 2013.

Whitmore, S. A.: Closed-form integrator for the quaternion (Euler angle) kinematics equations, US Patent 6,061,611, 2000.

Woodman, O. J.: An introduction to inertial navigation, University of Cambridge, Computer Laboratory, Technical Report. UCAMCL-TR-696, 14, 15, 2007.

Yalin, M. S.: An expression for bed-load transportation, Journal of the Hydraulics Division, 89, 221–250, 1963.

YEI, T.: 3-Space Sensor, User's Manual, YEI Technology, 2014.

Zekavat, R. and Buehrer, R. M.: Handbook of Position Location: Theory, Practice and Advances, vol. 27, John Wiley & Sons, 2011.

Zhao, F. and van Wachem, B.: A novel Quaternion integration approach for describing the behaviour of non-spherical particles, Acta Mechanica, 224, 3091–3109, 2013.

https://doi.org/10.5194/esurf-2020-20
Preprint. Discussion started: 3 April 2020

Earth Surface Dynamics Discussions

Data availability. The dataset is available upon request

Code availability. All the calculations were performed using the R-statistical software and specifically the libraries orientlib (Murdoch and Murdoch, 2015) for the rotation calculations and fitdistrplus (Delignette-Muller et al., 2015) for fitting statistical distributions. The code is open and freely available.

Author contributions. Georgios Maniatis performed the design and calibration of the sensor, the design and implementation of the experiments, all the physical and statistical calculations and produced the first draft of this paper. Trevor Hoey supervised the laboratory experiments, reviewed several versions of the manuscript and contributed significantly to the interpretation and contextualisation of the results. Rebecca Hodge contributed to the design of the laboratory experiments, reviewed several versions of the manuscript and contributed to the interpretation and contextualisation of the results. Dieter Rickenmann contributed to the design, supervised and assisted with the field experiments, reviewed several versions of the manuscript and contributed to the interpretation and contextualisation of the results. Alexandre Badoux contributed to the design of the field experiments and reviewed several versions of this manuscript.

Competing interests. The authors declare no competing interests

Acknowledgements. The flume experiments were contacted in the School of Engineering of the University of Glasgow. At the time of the flume experiments Georgios Maniatis (GM) was supported by a University of Glasgow Kelvin Smith Scholarship. The field experiments were supported by an Early Career Researcher award from the British Society for Geomorphology (2018). The authors thank Tim Montgomery (University of Glasgow) and Tobias Nicollier (WSL) for their assistance with the laboratory and field experiments, respectively. Finally, GM thanks Katerina Georgiou for her assistance with the design and production of the figures and the typewriting of the manuscript.

https://doi.org/10.5194/esurf-2020-20
Preprint. Discussion started: 3 April 2020

Earth Surface Dynamics
Discussions
Open Access

Appendix A: 3D IMU Measurements

https://doi.org/10.5194/esurf-2020-20
Preprint. Discussion started: 3 April 2020

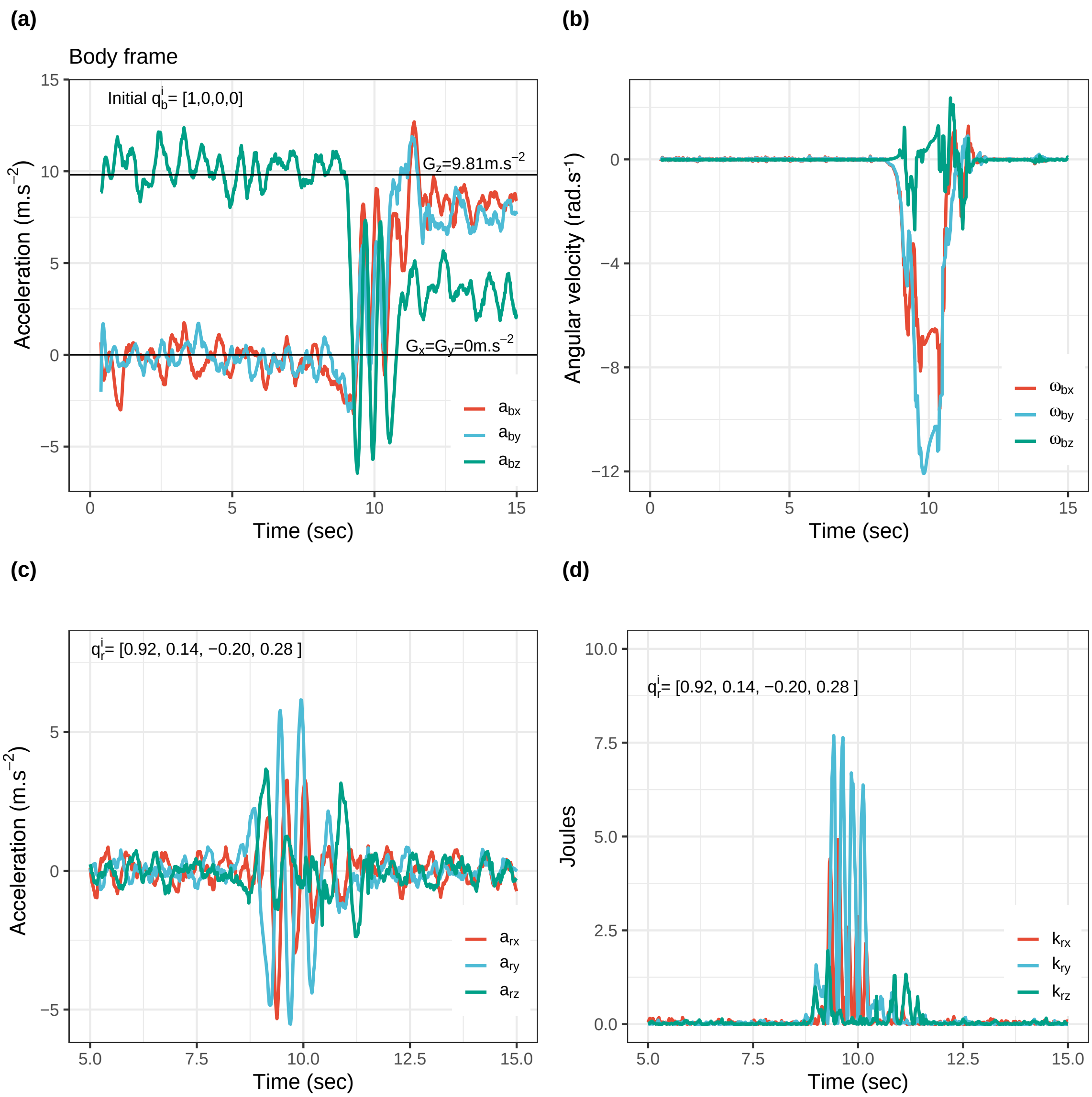

Figure A1. Example incipient motion IMU data. Measurements from the incipient motion experiments using the spherical sensor. **(a)** unfiltered and uncompensated inertial acceleration measurements. The sensor is initially aligned to gravity which results in the z axis of the accelerometer measuring a mean value of 9.81 m.sec^{-2}. **(b)** angular velocity (rad.sec^{-1}) measurements derived from the gyroscope. **(c)** linear acceleration along the three body frame axis. This is is the result of removing gravity from the inertial measurements shown in A and applying a FFT-high pass filter as described in Maniatis, 2016 (Chapter 6). **(d)** shows the kinetic energy calculation after integrating once the signal presented in (c) and applying the formula $K = \frac{1}{2}m\|v_r\|^2 + \frac{1}{2}I_{cm}\|\omega_b\|^2$ as described in Section 3.

https://doi.org/10.5194/esurf-2020-20
Preprint. Discussion started: 3 April 2020

Appendix B: Hydraulic parameters

B1 Flume experiments

https://doi.org/10.5194/esurf-2020-20
Preprint. Discussion started: 3 April 2020

Earth Surface Dynamics Discussions
Open Access

Table B1. The parameters are estimated as follows (based on the spherical particle geometry): ρ_p/ρ_f is the ratio of an experimental particle density to fluid density (ρ_f = 1000 kg.m^{-3}); P/D is the particle protrusion P (measured from the top of the surrounding fixed hemispheres to the top of the experimental particle). D is the particle diameter; S_b is bed slope; d is the flow depth (measured from the bottom of the bed to the water surface). $Ub{=}Q/A$ is the bulk mean velocity (Q is the flow rate and A is the cross sectional area of the flow); $R_b = (U_b d)/\nu$ is the bulk Reynolds number (where ν is the fluid kinematic viscosity at 25°C); $F = U_b/(gd)^{0.5}$ is the Froude number; B/d is the aspect ratio (B is the flume width); u_* is the shear velocity, estimated as $u_* = (\tau_b/\rho_f)^{0.5} = (gdS_b)^{0.5}$; τ_b is bed shear stress; and $R_* = (u_* d)/\nu$ is the friction Reynolds number. Shields number was calculated as $\tau_* = (\rho_f gHS)/[(\rho_p - \rho_f)gd_p]$. Finally the particle Reynolds number is estimated as $R_p = d_p u_*/\nu$

Experiment	ρ_p/ρ_f	P (m)	D (m)	P/D	S_b	B (m)	Flow increase (l/s^2)	Q (l/s)	d (m)	A (m^2)	U_b (m/s)	R_b	F	B/d	u_* (m/s)	τ_*	R_*	R_p
Flume	2.67	0.045	0.09	0.5	0.02	0.9	0.028	30	0.1	0.09	0.3	33300	0.336	9	0.140	0.013	14007	12606

https://doi.org/10.5194/esurf-2020-20
Preprint. Discussion started: 3 April 2020

B2 Field Experiments

Table B2. The parameters are estimated as follows: ρ_p/ρ_f is the ratio of an experimental particle density to fluid density (ρ_f = 1000 kg.m^{-3}); Q is the flow rate; d is the flow depth (measured from the bottom of the bed to the water surface); W is the channel width and S_b is bed slope. 0.105 (or 0.1) is also the average bedslope of the lowermost natural reach in Erlenbach of about 30 m length upstream of the stream gauging station; $F = U_b/(gd)^{0.5}$ is the Froude number; $R_b = (U_b d)/\nu$ is the bulk Reynolds number (where ν is the fluid kinematic viscosity at 0°C)

Experiment	ρ_p/ρ_f	Particle Long axis (m)	Particle Short axis (m)	Q (l/s)	d (m)	W (m)	S_b	U_b (m/s)	F	R_b
Erlenbach	2.67	0.10	0.07	120	0.15	3.5	0.1	0.22	0.19	770000

https://doi.org/10.5194/esurf-2020-20
Preprint. Discussion started: 3 April 2020

590 ## Appendix C: Summary histograms and correlation between lift and drag forces

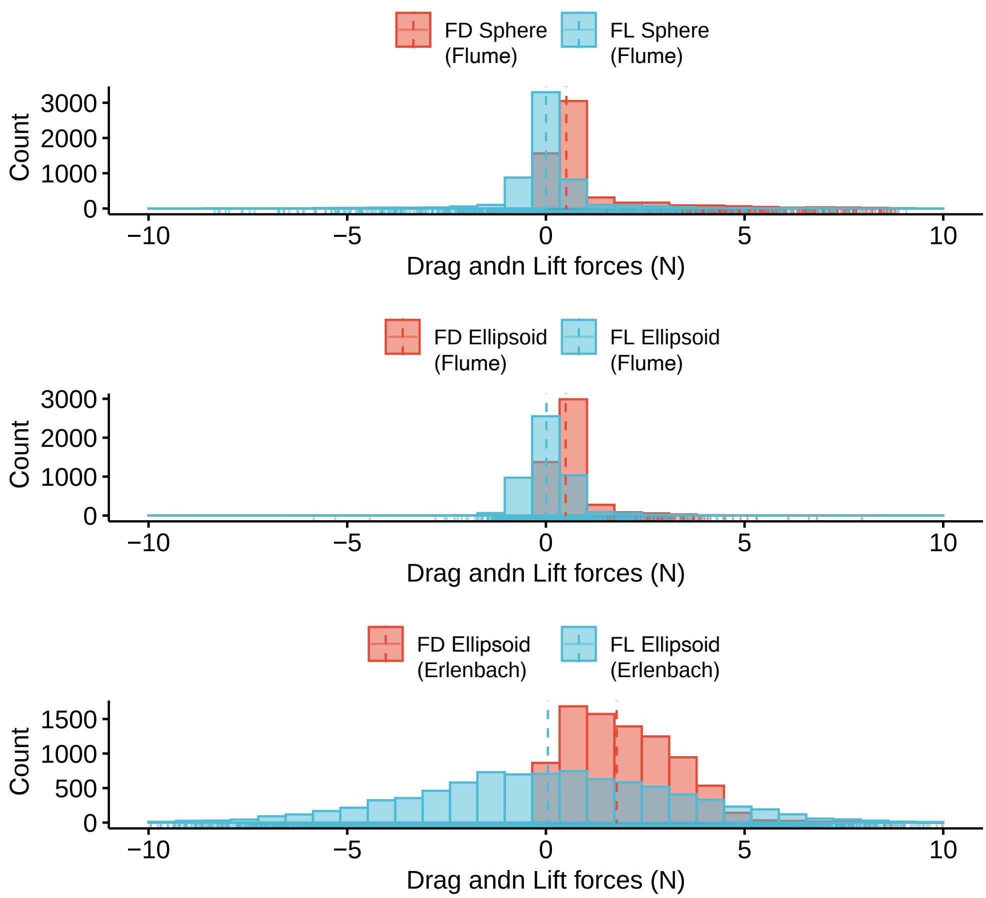

Figure C1. Histogram of inertial forces across from all experiments). The inertial dynamics show that lift forces (F_L) consistently fluctuate around zero while the drag forces (F_D) follow a heavy tail distribution which is a result of the vector addition of the resultant force components calculated parallel to the flume (Sphere and Ellipsoid) and the river (Erlenbach) plane (x_r - y_r plane, Section 4). The vertical lines indicate the corresponding medians.

https://doi.org/10.5194/esurf-2020-20
Preprint. Discussion started: 3 April 2020

Earth Surface Dynamics Discussions

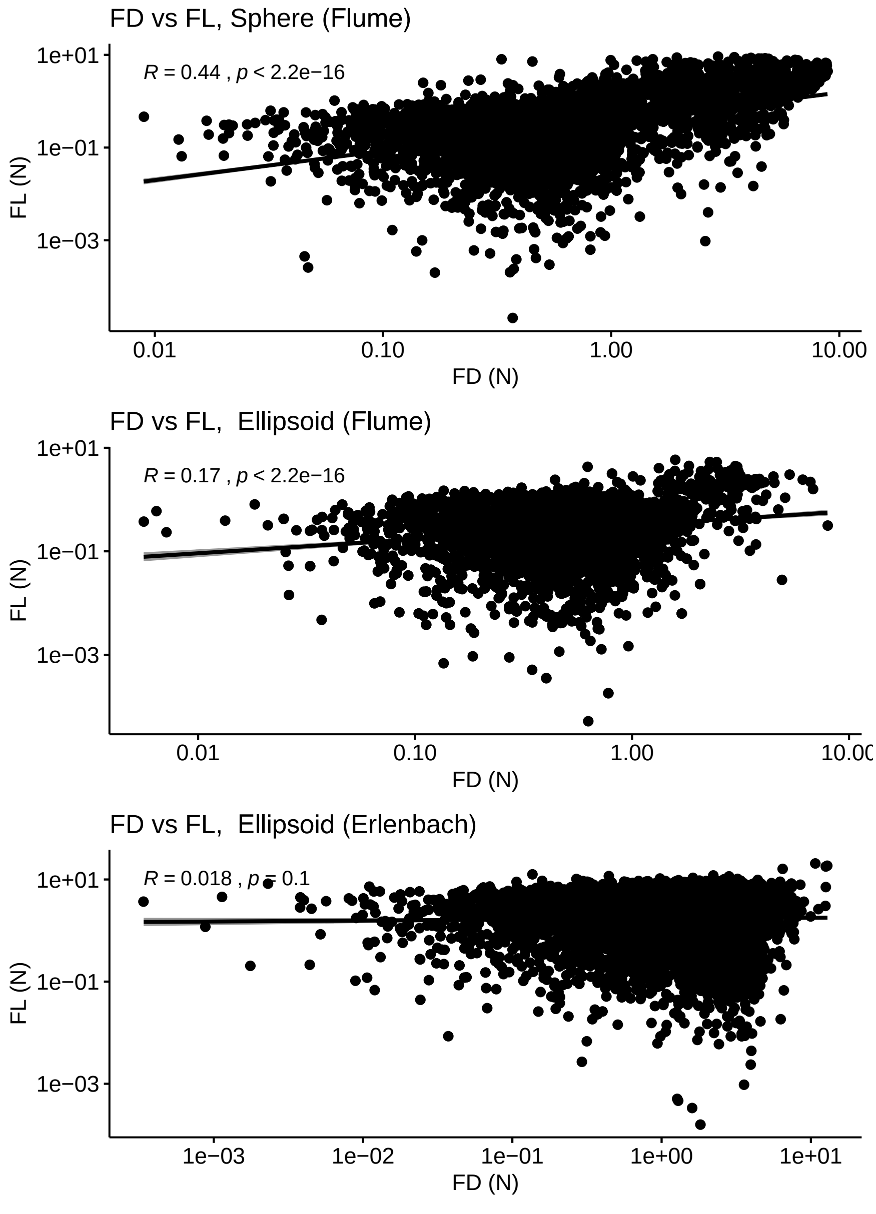

Figure C2. Lift vs Drag force magnitude correlation (flume experiments). Regression analysis applied on the magnitude of calculated forces (drag and lift) a moderate correlation for the spherical particle (statistically significant Pearson's R =0.44) and a weak correlation for the ellipsoid both in the laboratory and the field experiments (statistically significant Pearson's R =0.17 for the lab measurements, Ellipsoid, and not significant Pearson's R=0.018 for the field ones, Erlenbach). The latter supports the assumption of statistical independence between the two components for the ellipsoid, justifying the randomisation presented in Section 7 (Figure 6). The log scale was chosen to accommodate for the non-normal behaviour of the drag forces (Figure C1). Peason's R is an unbiased metric for this sample size, non-parametric Spearman's Rho gave very similar results.

https://doi.org/10.5194/esurf-2020-20
Preprint. Discussion started: 3 April 2020

Appendix D: Impulse: Selection of representative Drag and Lift distributions

Figure D1(a) shows the Cullen and Frey diagram for the identification of candidate distributions for the normalised Drag Impulses ($\hat{I}_{Drag}$). The skewness vs kurtosis relationship (blue dots), indicates a right tail distribution as a candidate. Figure D1 **(b)-(e)** show the graphical comparison between three candidate distributions (Weibull, gamma, and log-normal). Weibull and gamma distributions outperform the lognormal on the tails of the histogram (Q-Q plot), The median values are also captured better from the Weibull and gamma distributions (P-P plot). Finally, the histogram and CDF diagrams confirm that the log-normal distribution is the least representative of $\hat{I}_{Drag}$.

Figure D2 (a) shows the Cullen and Frey diagram for the identification of candidate distributions for the normalised lift impulses ($\hat{I}_{Lift}$). The skewness vs kurtosis relationship (blue dots), indicates a right tail distribution as a candidate. Figure D2 **(b)-(e)** show the graphical comparison between three candidate distributions (Weibull, gamma, and log-normal). The log-normal distribution outperforms the other candidates at the tail (Q-Q plot) and the median regions (P-P plot). Finally, the histogram and CDF diagrams confirm that the log-normal distribution is the best representative of $\hat{I}_{Lift}$.

https://doi.org/10.5194/esurf-2020-20
Preprint. Discussion started: 3 April 2020

Earth Surface Dynamics Discussions
Open Access
EGU

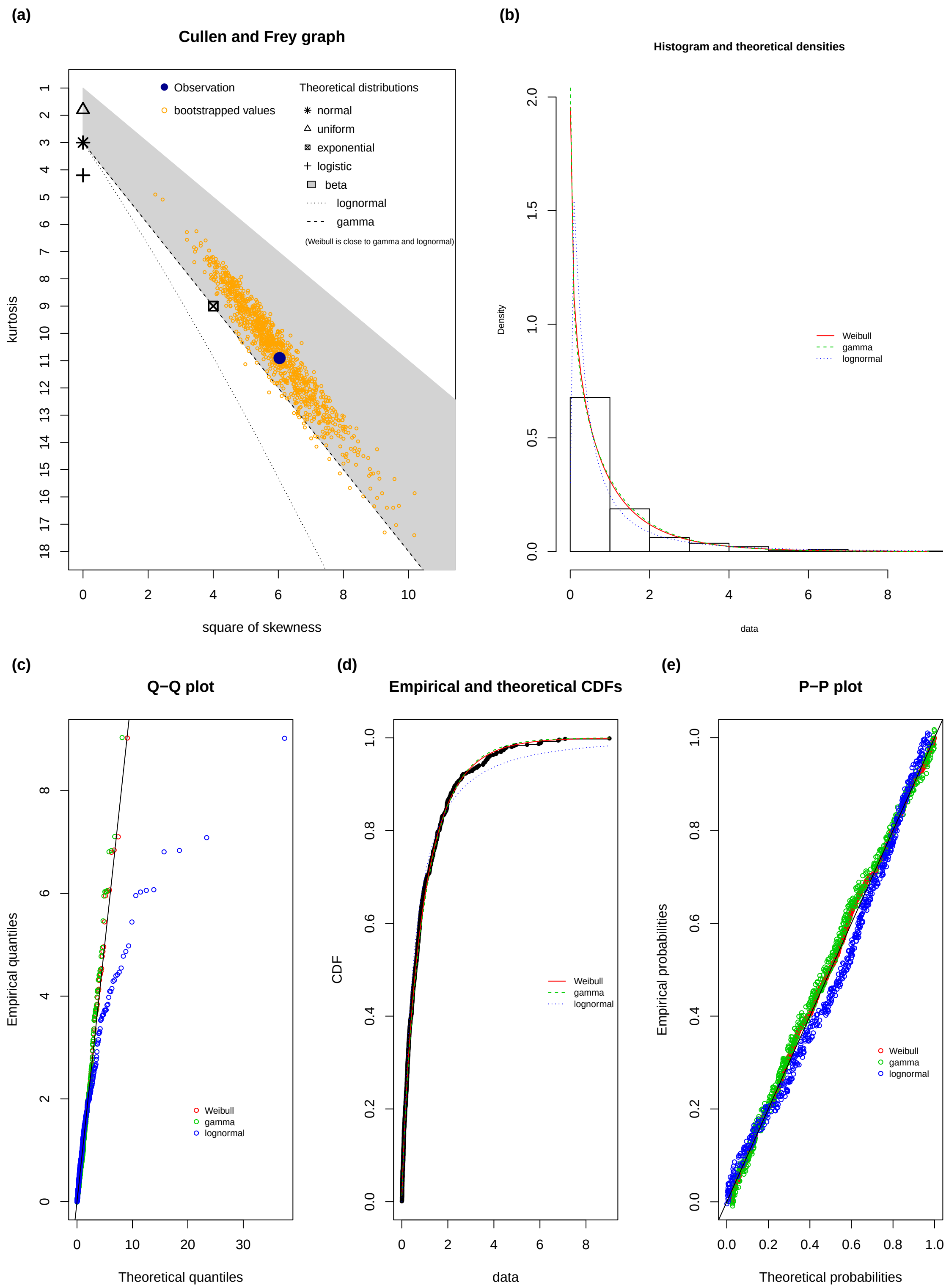

Figure D1. Choice of distribution for drag impulses

https://doi.org/10.5194/esurf-2020-20
Preprint. Discussion started: 3 April 2020

Earth Surface Dynamics
Discussions

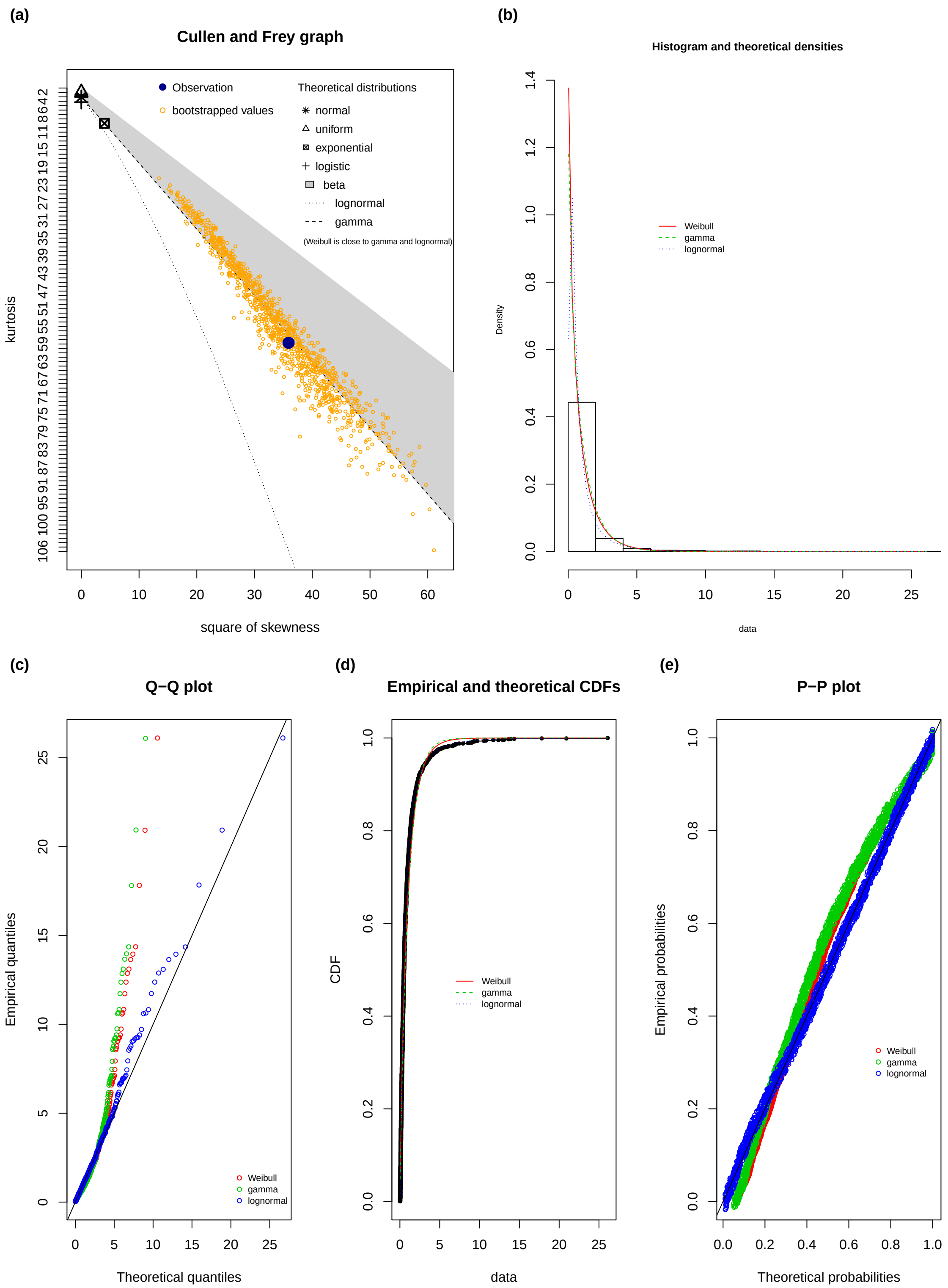

Figure D2. Choice of distribution for lift impulses

https://doi.org/10.5194/esurf-2020-20
Preprint. Discussion started: 3 April 2020

Table D1. Fitted Distribution statistics

Drag Impulses - Statistics for fitted distributions

Goodness-of-fit statistics	Weibull	gamma	Lnorm
Kolmogorov-Smirnov statistic	0.028	0.041	0.066
Cramer-von Mises statistic	0.068	0.196	0.665
Anderson-Darling statistic	0.577	1.244	4.227
Goodness-of-fit criteria			
Akaike's Information Criterion	1139	1145	1174
Bayesian Information Criterion	1148	1154	1183

Lift Impulses - Statistics for fitted distributions

Goodness-of-fit statistics	Weibull	gamma	Lnorm
Kolmogorov-Smirnov statistic	0.069	0.090	0.019
Cramer-von Mises statistic	3.571	6.057	0.093
Anderson-Darling statistic	26.4	34.9	0.9
Goodness-of-fit criteria			
Akaike's Information Criterion	3968	4042	3576
Bayesian Information Criterion	3979	4054	3588

Table D2. Statistics for selected distributions

Drag Impulses - Statistics for selected distribution (Weibull)

Parametric bootstrap medians and 95% percentile CI

	Median	2.5%	97.5%
shape	0.852	0.802	0.907
scale	0.916	0.831	1.010

Lift Impulses - Statistics for selected distribution (Lognormal)

Parametric bootstrap medians and 95% percentile CI

	Median	2.5%	97.5%
meaning	-0.663	-0.710	-0.614
sdlog	1.132	1.096	1.165

https://doi.org/10.5194/esurf-2020-20
Preprint. Discussion started: 3 April 2020

Earth Surface Dynamics Discussions

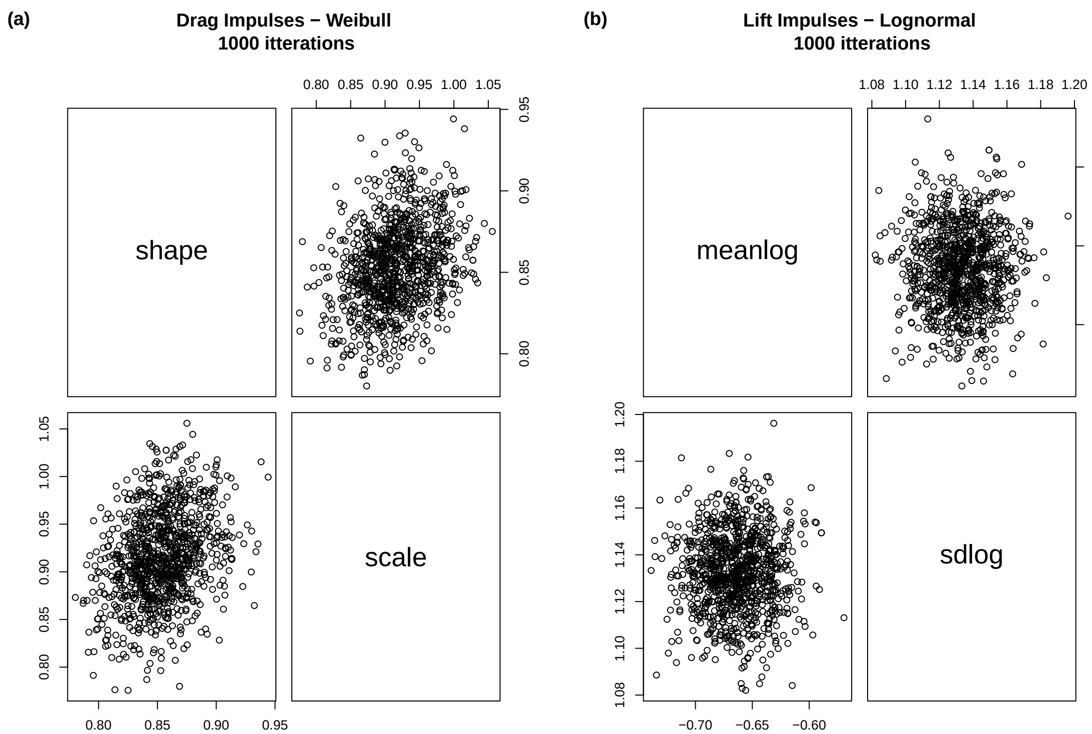

Figure D3. Bootstrap parameters for selected distributions The graphs quantify the stability of the selected distributions for drag and lift impulses. For the Weibull distribution (drag impulses) 1000 bootstrapped parameters were cross-compared, revealing a range of 0.22 for the shape parameter and 0.25 for the scale parameter **(a)**. For the Lognormal distribution (lift impulses) 1000 bootstrapped parameters were cross-compared, revealing a range of 0.15 for the log-mean parameter and 0.14 for log standard deviation parameter **(b)**. The differences are marginal, indicating good stability of the selected distributions for the scaling of the data.

https://doi.org/10.5194/esurf-2020-20
Preprint. Discussion started: 3 April 2020

Earth Surface Dynamics Discussions Open Access EGU

Appendix E: Quaternions and Rotations

E1 Summary Quaternion Algebra

Quaternions can be written in the form:

$$q = q_1 + q_2 i + q_3 j + q_4 k \tag{E1}$$

where q_1, q_2, q_3, q_4 are the components of quaternion q (and i, k, j unit imaginary numbers).

The quaternion conjugate is given by:

$$\bar{q} = q_1 - q_2 i - q_3 j - q_4 k \tag{E2}$$

The sum of two quaternions is then:

$$q + w = (q_1 + w_1) + (q_2 + w_2)i + (q_3 + w_3)j + (q_4 + w_4)k \tag{E3}$$

and quaternion multiplication is defined as:

$$\begin{aligned} q \bigotimes w \quad = \quad & (q_1 w_1 - q_2 w_2 - q_3 w_3 - q_4 w_4) + (q_1 w_2 + q_2 w_1 + q_3 w_4 - q_4 w_3)i \\ & + (q_1 w_3 - q_2 w_4 + q_3 w_1 + q_4 w_2)j + (q_1 w_4 + q_2 w_3 - q_3 w_2 + q_4 w_1)k. \end{aligned} \tag{E4}$$

The quaternion norm is therefore defined by:

$$n(q) = \sqrt{\bar{q}q} = \sqrt{q_2^2 + q_1^2 + q_3^2 + q_4^2} \tag{E5}$$

https://doi.org/10.5194/esurf-2020-20
Preprint. Discussion started: 3 April 2020

With little manipulation, the quaternions can be directly related to four-element vectors.

Quaternions can be interpreted as a scalar plus a vector by writing:

$$q = q_1 + q_2 i + q_3 j + q_4 k = (s, \hat{v}) \tag{E6}$$

where $s = q_1$ and $\hat{v} = q_2 i + q_3 j + q_4 k$. In this notation, quaternion multiplication has the form:

$$\begin{aligned} q_1 \bigotimes q_2 &= (s_1, \hat{v}_1) \cdot (s_2, \hat{v}_2) \\ &= (s_1 s_2 - \hat{v}_1 \cdot \hat{v}_2, s_1 \hat{v}_2 + s_2 \hat{v}_1 + \hat{v}_1 \cdot \hat{v}_2) \end{aligned} \tag{E7}$$

Finally, the rotation about the unit vector $\hat{n}$ by an angle θ can be computed using the quaternion:

$$q = (s, v) = (\cos(\frac{1}{2}\theta), \hat{n}\sin(\frac{1}{2}\theta)) \tag{E8}$$

The components of this quaternion are called Euler parameters. After rotation, a point $p = (0, p)$ is then given by:

$$p' = qpq^{-1} = qp\bar{q} \tag{E9}$$

since $n(q) = 1$.

A concatenation of two rotations, first q_1 and then q_2, can be computed using the identity:

$$q_2(q_1 p \bar{q_1})\bar{q_2} = (q_2 q_1) p (\bar{q_1}\bar{q_2}) = (q_2 q_1) p \overline{q_2 q_1} \tag{E10}$$

Finally, the transformation that gives the equivalent DCM for a quaternion $q = q_1 + q_2 i + q_3 j + q_4 k$, is given by:

https://doi.org/10.5194/esurf-2020-20
Preprint. Discussion started: 3 April 2020

$$\begin{aligned}R(q) \quad = \quad & [q_1^2+q_2^2-q_3^2-q_4^2, 2(q_2q_3-q_4q_1), 2(q_2q_4+q_3q_1)\\ & 2(q_2q_3+q_4q_1), q_1^2-q_2^2+q_3^2-q_4^2, 2(q_3q_4-q_2q_1)\\ & 2(q_2q_4-q_3q_1), 2(q_3q_4+q_2q_1), q_1^2-q_2^2-q_3^2+q_4^2] \qquad \text{(E11)}\end{aligned}$$

655

E2 The Gimbal lock (adapted from Maniatis, 2016)

To demonstrate the advantage of quaternions we rotate randomly the static vector of gravity. In an orthogonal Cartesian frame where the origin of the z-axis is the centre of the Earth, gravity is measured as $[G_x, G_y, G_z] = [0, 0, 9.81]$ m.sec^{-2}. If we assume a rigid body rotating freely and randomly in this frame we can do the rotation calculations. Avoiding further mathematisation,
660 the series of the calculations is the following:

- Randomisation of the body frame angular velocities of the rigid body ω_x,ω_y,ω_z in a $[-2\pi, 2\pi]$ range. A frequency of 100 Hz is used.
- Calculation of successive quaternions using direct multiplication for random angular velocities.
- Calculate the Direction Cosine Matrix from Euler angles.
665 – Rotate the vector of gravity in the body frame of the rigid body using both of the Direction Cosine Matrix using common matrix vector multiplication.

The vector expressed in the body frame is shown in Figure E1. The results are different and Gimbal lock (an inconsistent axis change when the second rotation approaches $\pm\pi/2$) occurs after the 450^{th} iteration which corresponds to 8 sec in simulation time.

https://doi.org/10.5194/esurf-2020-20
Preprint. Discussion started: 3 April 2020

Earth Surface Dynamics Discussions
Open Access
EGU

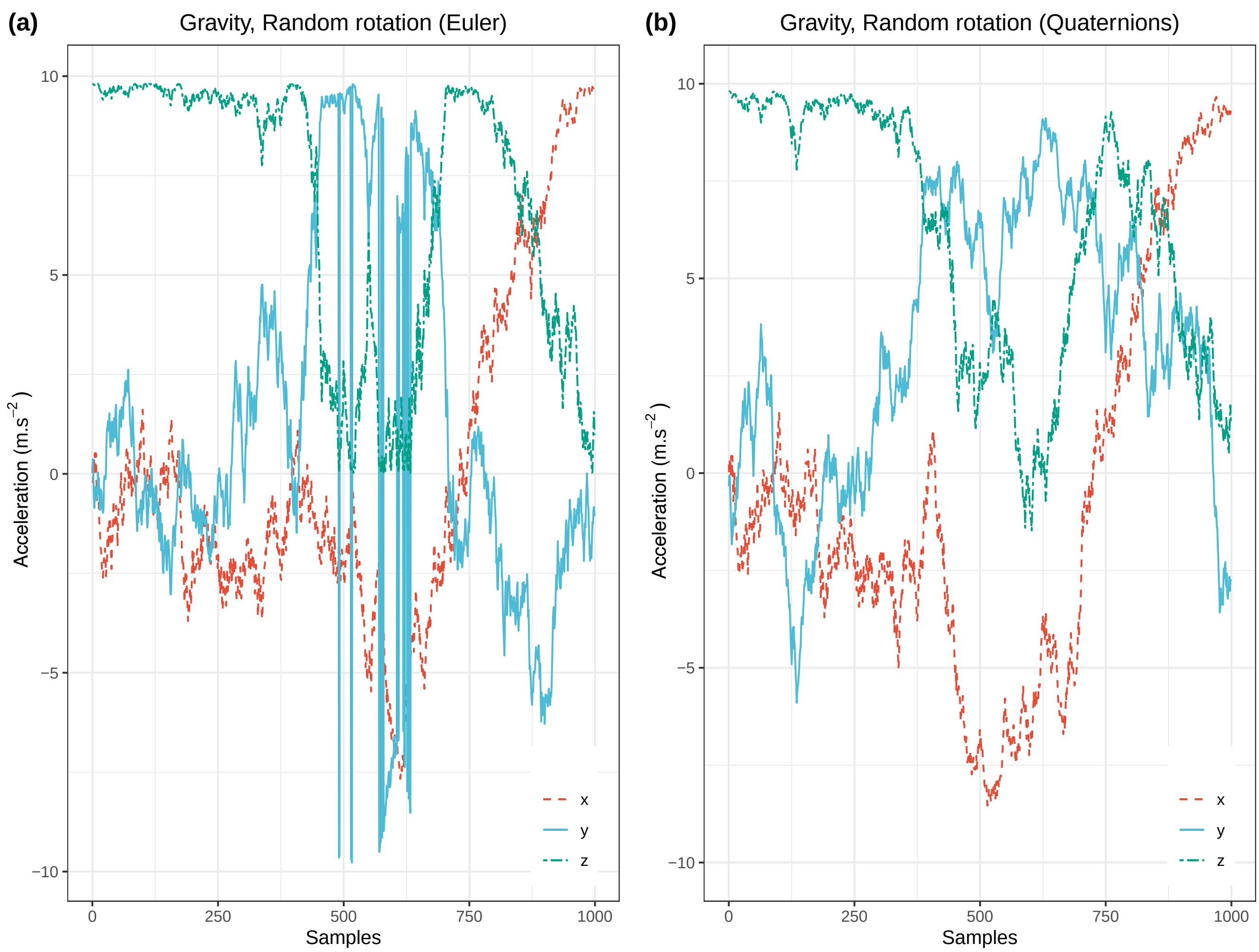

Figure E1. Random rotation of the static vector of Gravity. $[g_x, g_y, g_z] = [0, 0, 9.81]$ m.s^{-2} in the gravity frame of reference as expressed in the body frame of randomly rotating rigid body ($dt = 0.01$ sec). a. demonstrates the rotation calculations with the usage of Euler angles. Gimbal lock occurs after the 400 iterations. b. shows the same rotation series calculated via quaternions. No Gimbal lock occurs and the result is easy to interpret as it is based on the use of the measured body frame angular velocities.